iScience

CellPress
OPEN ACCESS

Article

# Respiratory infection with influenza A virus delays remyelination and alters oligodendrocyte metabolism

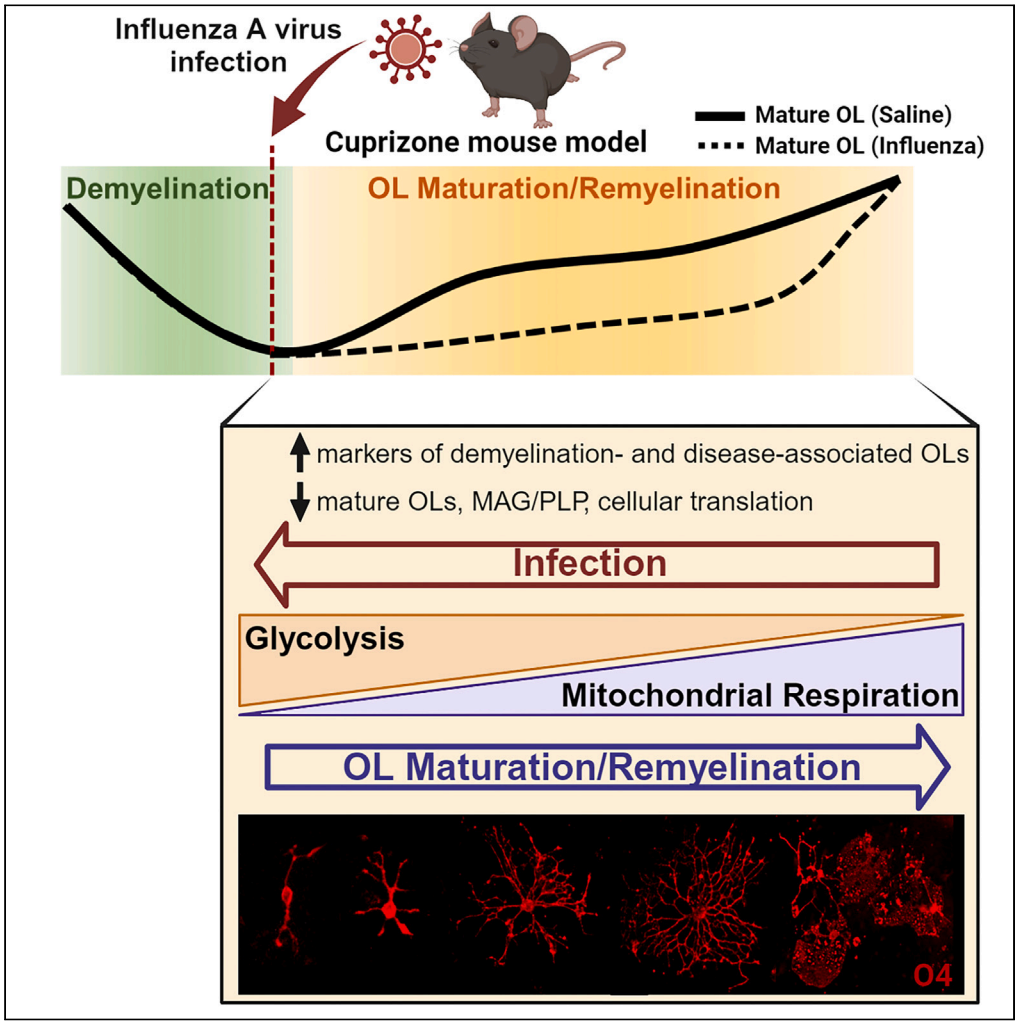


Allison Y. Louie, Jenny Drnevich, Jennifer L. Johnson, Meagan Woodard, Anna V. Kukekova, Rodney W. Johnson, Andrew J. Steelman

asteelma@illinois.edu

## Highlights

Spatial transcriptomics revealed effects of flu infection on remyelination

Flu perpetuated a demyelination transcriptional signature and delayed remyelination

Flu increased glycolytic capacity and suppressed translation of oligodendrocytes

Oligodendrocytes increased mitochondrial respiration during (re) myelination

Louie et al., iScience 27, 110464
August 16, 2024 
https://doi.org/10.1016/j.isci.2024.110464

iScience

CellPress
OPEN ACCESS

Article

# Respiratory infection with influenza A virus delays remyelination and alters oligodendrocyte metabolism

Allison Y. Louie,[1] Jenny Drnevich,[2] Jennifer L. Johnson,[3] Meagan Woodard,[3] Anna V. Kukekova,[3] Rodney W. Johnson,[1,3,4] and Andrew J. Steelman[1,3,4,5,6,*]

## SUMMARY

**Peripheral viral infection disrupts oligodendrocyte (OL) homeostasis such that endogenous remyelination may be affected. Here, we demonstrate that influenza A virus infection perpetuated a demyelination- and disease-associated OL phenotype following cuprizone-induced demyelination that resulted in delayed OL maturation and remyelination in the prefrontal cortex. Furthermore, we assessed cellular metabolism *ex vivo*, and found that infection altered brain OL and microglia metabolism in a manner that opposed the metabolic profile induced by remyelination. Specifically, infection increased glycolytic capacity of OLs and microglia, an effect that was recapitulated by lipopolysaccharide (LPS) stimulation of mixed glia cultures. In contrast, mitochondrial dependence was increased in OLs during remyelination, which was similarly observed in OLs of myelinating P14 mice compared to adult and aged mice. Collectively, our data indicate that respiratory viral infection is capable of suppressing remyelination, and suggest that metabolic dysfunction of OLs is implicated in remyelination impairment.**

## INTRODUCTION

It is well established that systemic inflammation can trigger glial activation.[1,2] For instance, respiratory infection with a non-neurotropic strain of influenza A virus induces pro-inflammatory glial profiles,[3–5] which coincides with the suppression of transcripts and proteins required for oligodendrocyte (OL) maturation and myelin generation.[6] Moreover, treatment with colony stimulating factor 1 receptor antagonist during infection partially alleviates changes to OL-specific transcripts,[6] implicating a role for reactive microglia in this process. A similar phenomenon has been observed during experimental SARS-CoV-2 infection.[7] These observations are likely of clinical significance since alterations to OL homeostasis resulting from respiratory viral infection may contribute to neurological sequelae, such as cognitive impairments that have been documented to occur within infected adults.[8–10]

Similarly, changes to OL homeostasis may affect remyelination potential in persons with multiple sclerosis (MS), an inflammatory, demyelinating disease of the central nervous system (CNS) and major cause of non-traumatic neurological disability in young people. The majority of persons with MS exhibit a disease course that is characterized by repeated bouts of inflammatory episodes with intermittent periods of recovery, termed relapsing-remitting MS. While the triggers of relapse remain an enigma, increased relapse frequency may also reduce remyelination capacity.[11] Indeed, evidence suggests that excessive inflammation creates a remyelination-hostile environment.[12–17] This is of importance as studies performed in animal models indicate that remyelination can restore proper signal conduction, prevent axonal injury, and promote recovery of function.[18–20] Yet, a hallmark feature of MS is the incomplete regeneration of myelin following inflammatory demyelination, especially during progressive disease.

Whether respiratory viral infection can act to influence endogenous remyelination is currently unknown. Given that peripheral viral infections can disrupt OL homeostasis, we hypothesized that respiratory influenza infection could affect endogenous remyelination capacity following acute cuprizone (CPZ)-induced demyelination, a well-characterized and highly reproducible model that allows for the study of remyelination. We found that influenza A virus infection occurring during peak demyelination perpetuated a demyelination- and disease-associated OL phenotype and delayed both OL maturation and remyelination in the prefrontal cortex, as indicated by spatial transcriptomics and histological analyses. Moreover, we found that infection altered brain OL and microglia metabolism in a manner that opposed the metabolic profile induced by remyelination. Specifically, infection increased glycolytic capacity of OLs and microglia, an effect that was recapitulated in

[1]Neuroscience Program, University of Illinois at Urbana-Champaign, Urbana, IL, USA
[2]Roy J. Carver Biotechnology Center, University of Illinois at Urbana-Champaign, Urbana, IL, USA
[3]Department of Animal Sciences, University of Illinois at Urbana-Champaign, Urbana, IL, USA
[4]Division of Nutritional Sciences, University of Illinois at Urbana-Champaign, Urbana, IL, USA
[5]Carl R. Woese Institute for Genomic Biology, University of Illinois at Urbana-Champaign, Urbana, IL, USA
[6]Lead contact
*Correspondence: asteelma@illinois.edu
https://doi.org/10.1016/j.isci.2024.110464

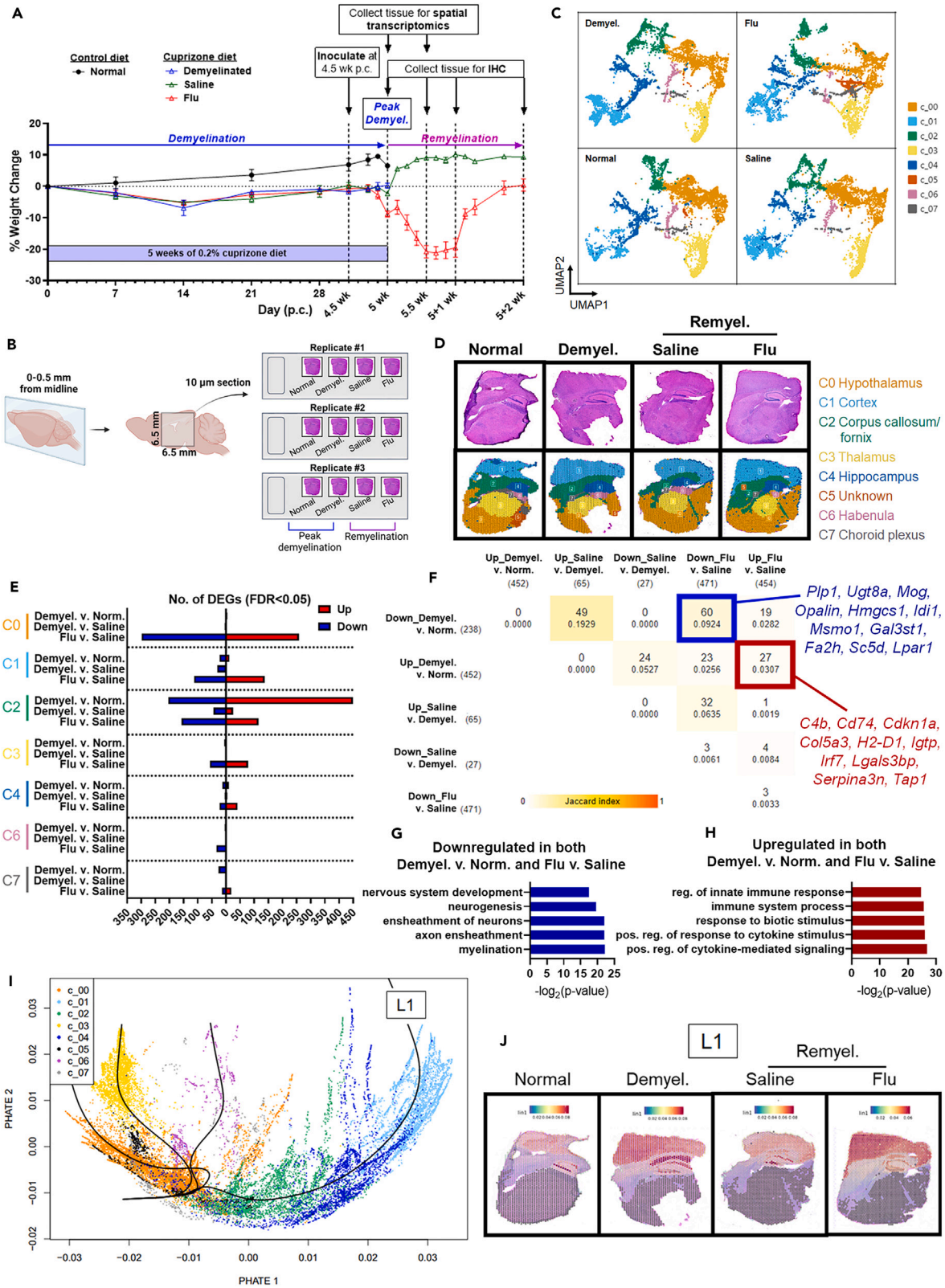
A
Collect tissue for spatial transcriptomics
Inoculate at 4.5 wk p.c.
Collect tissue for IHC
Peak Demyel.
Control diet
Normal
Cuprizone diet
Demyelinated
Saline
Flu
Demyelination
Remyelination
% Weight Change
5 weeks of 0.2% cuprizone diet
Day (p.c.)
4.5 wk
5 wk
5.5 wk
5+1 wk
5+2 wk
C
Demyel.
Flu
Normal
Saline
c_00
c_01
c_02
c_03
c_04
c_05
c_06
c_07
UMAP2
UMAP1
B
0-0.5 mm from midline
10 µm section
6.5 mm
6.5 mm
Replicate #1
Replicate #2
Replicate #3
Normal
Demyel.
Saline
Flu
Peak demyelination
Remyelination
D
Remyel.
Normal
Demyel.
Saline
Flu
C0 Hypothalamus
C1 Cortex
C2 Corpus callosum/ fornix
C3 Thalamus
C4 Hippocampus
C5 Unknown
C6 Habenula
C7 Choroid plexus
E
No. of DEGs (FDR<0.05)
Up
Down
C0
C1
C2
C3
C4
C6
C7
Demyel. v. Norm.
Demyel. v. Saline
Flu v. Saline
F
Up_Demyel. v. Norm. (452)
Up_Saline v. Demyel. (65)
Down_Saline v. Demyel. (27)
Down_Flu v. Saline (471)
Up_Flu v. Saline (454)
Down_Demyel. v. Norm. (238)
Up_Demyel. v. Norm. (452)
Up_Saline v. Demyel. (65)
Down_Saline v. Demyel. (27)
Down_Flu v. Saline (471)
Jaccard index
Plp1, Ugt8a, Mog, Opalin, Hmgcs1, Idi1, Msmo1, Gal3st1, Fa2h, Sc5d, Lpar1
C4b, Cd74, Cdkn1a, Col5a3, H2-D1, Igtp, Irf7, Lgals3bp, Serpina3n, Tap1
G
Downregulated in both Demyel. v. Norm. and Flu v. Saline
nervous system development
neurogenesis
ensheathment of neurons
axon ensheathment
myelination
-log2(p-value)
H
Upregulated in both Demyel. v. Norm. and Flu v. Saline
reg. of innate immune response
immune system process
response to biotic stimulus
pos. reg. of response to cytokine stimulus
pos. reg. of cytokine-mediated signaling
-log2(p-value)
I
L1
PHATE 1
PHATE 2
J
L1
Remyel.
Normal
Demyel.
Saline
Flu

**Figure 1. Spatial transcriptomic analysis revealed region-dependent transcriptional changes attributable to demyelination, remyelination, and infection**

(A) Experimental schematic showing endpoints and percent weight change over time (p.c. = post-cuprizone). Data are from three independent experiments and are represented as mean ± SEM.

(B) Experimental schematic of brain tissues collected for spatial transcriptomics.

(C) UMAP plot of 8 distinguished clusters across four conditions. $n = 3$ animals per condition.

(D) Representative images of H&E stained tissues of each condition overlaid with spatially resolved transcriptomes and corresponding cluster identities.

(E) Number of up- and downregulated differentially expressed genes (DEGs) with false discovery rate (FDR) < 0.05 for Demyelinated v. Normal, Demyelinated v. Saline, and Flu v. Saline contrasts.

(F) Number of up- and downregulated DEGs shared between each contrast shown in E. Data were collapsed across clusters to assess global effect of demyelination, remyelination, and infection. Matrix generated using molbiotools.com

(G and H) Top five significant gene ontology terms associated with DEGs that were (G) downregulated or (H) upregulated in both Demyelinated v. Normal and Flu v. Saline contrasts.

(I) PHATE trajectory analysis of top 3000 most differentially expressed genes across all conditions.

(J) Representative tissue sections of each condition overlaid with heatmap values from lineage 1 (L1) of PHATE analysis.

primary mixed glial cultures undergoing an inflammatory challenge. In contrast, mitochondrial respiration was increased in OLs during remyelination, which was similarly observed in OLs isolated from brains of myelinating P14 mice compared to adult and aged mice. Collectively, these data indicate that respiratory viral infection is capable of suppressing remyelination, and implicate OL metabolic dysfunction as a contributing factor.

## RESULTS

### Spatial transcriptomic analysis revealed region-dependent transcriptional changes attributable to demyelination, remyelination, and infection

Intoxication by CPZ causes demyelination to occur in anatomically distinct regions of the brain,[21] and these regions undergo repair in a manner that is also temporally distinct. Thus, to test whether infection could alter the remyelination process, we performed Visium spatial transcriptomics on brains from non-CPZ controls ("Normal"), CPZ-fed mice at peak demyelination ("Demyelinated"), and saline-inoculated ("Saline") or influenza virus-inoculated ("Flu") mice during active remyelination (Figures 1A and 1B). In this manner, peak sickness as indicated by weight loss due to infection coincided with partial remyelination at 5 + 0.5 weeks (Figure 1A). Sequencing resulted in 23,963 total tissue-covered spots from all four conditions (Figure 1C). Clustering analysis resulted in eight clusters (numbered 0–7) that colocalized with known brain regions, of which we identified by histology hypothalamus, cortex, corpus callosum (CC)/fornix, thalamus, hippocampus, habenula, and choroid plexus (Figure 1D; Table S1). We performed six pairwise comparisons for each cluster with a raw $p$ value threshold of <0.001 (Table S2), except for cluster 5 which predominately represented cells from one Flu replicate. We further filtered differentially expressed genes (DEGs) by a false discovery rate (FDR) cutoff of 0.05 and focused on three main contrasts for each cluster: "Demyelinated vs. Normal" to assess the effect of demyelination, "Demyelinated vs. Saline" to assess the effect of remyelination, and "Flu vs. Saline" to assess the effect of infection during remyelination (Figure 1E). The transcriptional effect of demyelination was most prominent in the CC/fornix (653 DEGs) followed by cortex (35 DEGs) (Figure 1E). Likewise, the transcriptional effects of remyelination was greatest in the CC/fornix (69 DEGs) and cortex (39 DEGs) (Figure 1E). The effect of infection was most prominent in the hypothalamus, CC/fornix, and cortex with 556, 272, and 250 DEGs between Flu and Saline groups, respectively (Figure 1E). To assess any similarities in the transcriptional changes caused by demyelination, remyelination, and infection, we collapsed clusters and compared DEGs from each of the three contrasts (Figure 1F). Unsurprisingly, a large number of genes that were downregulated by demyelination were also upregulated during the remyelination process (49 shared DEGs; Figure 1F). Many genes initially downregulated by demyelination remained downregulated in mice inoculated with IAV compared to those inoculated with saline (60 shared DEGs; Figure 1F). These downregulated genes included myelin protein transcripts such as *Plp1*, *Ugt8a*, and *Mog* and cholesterol biosynthesis genes such as *Hmgcs1*, *Idi1*, and *Msmo1* (Figure 1F; Table S3). Gene ontology (GO) enrichment analysis confirmed that DEGs downregulated by both demyelination and infection were associated with the terms *myelination* and *axon ensheathment* (Figure 1G). Notably, the vast majority of these genes (57/60, 95%) were previously found to be downregulated by bulk-seq analysis of CNS tissues from flu-inoculated mice compared to saline-inoculated controls.[6] Likewise, the majority of genes upregulated by both demyelination and infection conditions in the current dataset (25/27, 93%) were upregulated by infection compared to saline in our previous bulk-seq dataset.[5] Upregulated genes included *Cdkn1a*, *Serpina3n*, and *Col5a3*, which were recently identified as markers of demyelination-associated OLs in a snRNA-seq analysis of CC/cortex tissue following CPZ-induced demyelination.[22] GO analysis of upregulated genes revealed association with *cytokine signaling* and *immune response* pathways (Figure 1H). These data indicate that during remyelination, infection perpetuated a demyelination-associated transcriptional profile in accordance with that observed in previous studies with infection alone.

To visualize spatially resolved patterns within our dataset, we utilized PHATE analysis,[23] which is a dimensionality reduction method that is particularly useful for preserving continuous relationships between cells, such as the progression of OL differentiation, followed by trajectory analysis in Slingshot. PHATE/Slingshot analysis using the 3000 most variable genes within our dataset resulted in a lineage tree of four main trajectories (Figure 1I). Lineage 1 (L1) was the most striking as it comprised cortex, CC/fornix, and hippocampus clusters (Figure 1I), all of which are major regions known to demyelinate and subsequently remyelinate in the CPZ model.[24–27] Notably, visualization of L1 as a heatmap on the Visium tissue sections (Figure 1J) revealed strong transcriptional changes occurring in the medial CC starting caudal to the fornix in mice of the

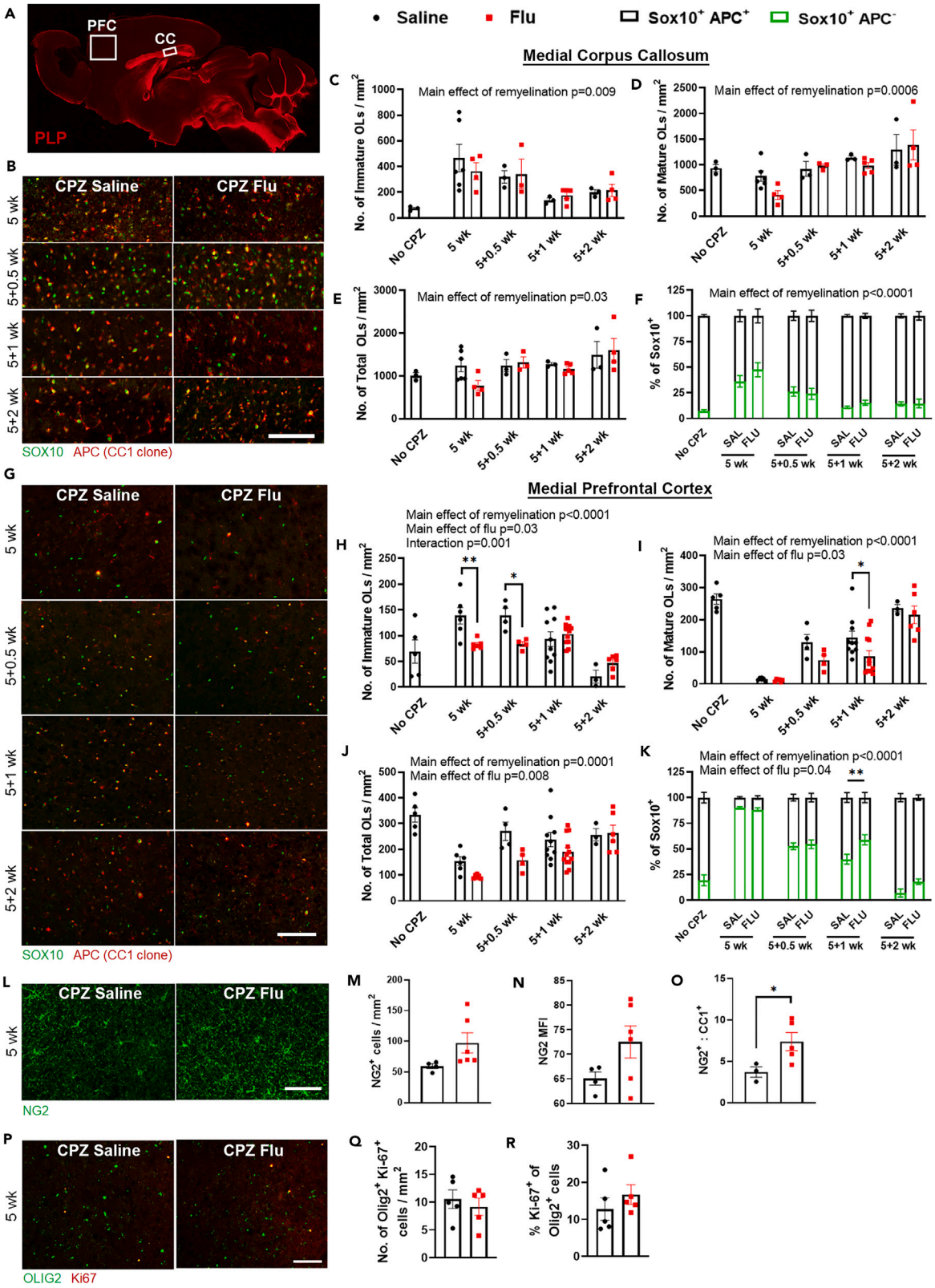
A
PFC
CC
PLP
B
CPZ Saline
CPZ Flu
5 wk
5+0.5 wk
5+1 wk
5+2 wk
SOX10 APC (CC1 clone)
Saline
Flu
Sox10+ APC+
Sox10+ APC-
Medial Corpus Callosum
C
Main effect of remyelination p=0.009
No. of Immature OLs / mm2
D
Main effect of remyelination p=0.0006
No. of Mature OLs / mm2
E
Main effect of remyelination p=0.03
No. of Total OLs / mm2
F
Main effect of remyelination p<0.0001
% of Sox10+
No CPZ
SAL
FLU
Medial Prefrontal Cortex
H
Main effect of remyelination p<0.0001
Main effect of flu p=0.03
Interaction p=0.001
I
Main effect of remyelination p<0.0001
Main effect of flu p=0.03
J
Main effect of remyelination p=0.0001
Main effect of flu p=0.008
K
Main effect of remyelination p<0.0001
Main effect of flu p=0.04
G
CPZ Saline
CPZ Flu
SOX10 APC (CC1 clone)
L
NG2
M
NG2+ cells / mm2
N
NG2 MFI
O
NG2+ : CC1+
P
OLIG2 Ki67
Q
No. of Olig2+ Ki-67+ cells / mm2
R
% Ki-67+ of Olig2+ cells

**Figure 2. Infection decreased the number of mature OLs in the mPFC during remyelination**

(A) PLP-stained sagittal brain section depicting the relative locations of the medial PFC (mPFC) and medial corpus callosum immediately caudal to the fornix (CC).
(B) SOX10 and APC (CC1 clone) immunofluorescence in the CC.
(C–E) Number of (C) immature OLs ($SOX10^+APC^-$), (D) mature OLs ($SOX10^+APC^+$), and (E) total OLs ($SOX10^+$) in the CC.
(F) Proportion of immature and mature OLs of total OLs in the CC.
(G) SOX10 and APC (CC1 clone) immunofluorescence in the mPFC.
(H–J) Number of (H) immature OLs, (I) mature OLs, and (J) total OLs in the mPFC.
(K) Proportion of immature and mature OLs of total OLs in the mPFC. For B–K, n = 3–12 animals per condition per time point.
(L) NG2 (CSPG4) immunofluorescence in the mPFC.
(M) Number of NG2+ cells, (N) NG2 mean fluorescent intensity (MFI), and (O) ratio of NG2 to APC $(CC1)^+$ cells in the mPFC at 5 weeks p.c. For L–O, n = 3–6 animals per condition.
(P) OLIG2 and Ki67 immunofluorescence in the mPFC.
(Q) Number and (R) proportion of $Ki67^+$ OLs in the mPFC.
For P–R, *n* = 5 animals per condition. Data analyzed by two-way ANOVA with Bonferroni correction, except L–R for which Student's t test was performed. Data presented as mean ± SEM. "No CPZ" reference group was excluded from statistical analysis. $*p < 0.05$, $**p < 0.01$. All scale bars represent 100μm.

Demyelinated group, which is a distinct feature of CPZ-induced demyelination.[21,28] These transcriptional changes were dramatically reduced in the CC of the remyelinating tissues and were not present in tissues from mice in the Normal group (Figure 1J). The same transcriptomic signature was apparent within the cortex of Demyelinated and Flu mice in a caudal-to-rostral manner, and to a much lesser degree in the cortex of Normal or Saline mice (Figure 1J). These data suggest that infection prolonged the transcriptional changes induced by demyelination, and that these changes resolved in a caudal-to-rostral manner.

Since our analysis indicated that the cortex and CC were most affected by both demyelination and infection (Figures 1E and 1J), we focused on these regions for subsequent analyses. Although infection induced many demyelination-associated transcriptional changes (Figures 1F–1J), the genes most highly upregulated by infection compared to saline ($log_2FC > 1$, FDR<0.05) in either cortex or CC/fornix clusters during remyelination were predominately specific to infection and not upregulated by demyelination, at least at 5 weeks (Table S3). GO analysis revealed these genes were associated with *response to interferon gamma* ($p = 0.0069$, data not shown), which is in line with our previous finding that the most prominent upregulated genes in the CNS during influenza infection are controlled by IFN signaling.[5] Many of these infection-induced genes including *Plin4*, *Hif3a*, and *Sult1a1* (Table S3) were identified as markers of disease-associated OLs in multiple mouse models of inflammatory demyelination as well as human MS, including a disease-associated OL signature defined by response to interferon.[29,30]

Collectively, these data indicate that infection prolonged the transcriptional effect of demyelination as well as upregulated markers of disease-associated OLs during remyelination.

## Infection decreased the number of mature OLs and myelin density in the mPFC during remyelination

To confirm that infection suppressed OL maturation, we quantified the number of both mature and immature OLs over the course of remyelination within regions of interest—the medial CC immediately caudal to the fornix and the medial prefrontal cortex (mPFC) (Figure 2A). In both regions we observed an effect of remyelination characterized by peak numbers of immature OLs at 5 weeks post-cuprizone (p.c.), which gradually declined, coinciding with a complementary increase in numbers of mature OLs (Figures 2B–2D, 2G–2I). However, in the CC (Figure 2B), infection neither altered the number of immature OLs ($SOX10^+APC^-$, Figure 2C), mature OLs ($SOX10^+APC^+$, Figure 2D), or total OLs ($SOX10^+$, Figure 2E) nor the proportions of immature and mature OLs of the total OL population (Figure 2F). In contrast, infection decreased the number of immature OLs at 5 weeks and 5 + 0.5 weeks as well as the number of mature OLs at 5+1 week in the mPFC (Figures 2G–2I). At 5+1 week, a time point corresponding to substantial remyelination, the number of total OLs was not different between Saline and Flu groups (Figure 2J). However, the proportion of immature OLs was greater in the infected mice (Figure 2K), suggesting an effect of infection on OL maturation in the mPFC.

Since the number of immature OLs was decreased by flu in the mPFC at 5 weeks p.c., we asked whether the number of $NG2^+$ glia was affected by flu in this region at this time point (Figure 2L). Neither number of $NG2^+$ cells nor NG2 MFI was significantly altered (Figures 2M and 2N), however, the ratio of $NG2^+$ to $CC1^+$ cells was increased by infection by 5 weeks p.c. (Figure 2O). In addition, the number ($OLIG2^+Ki67^+$ cells) and proportion of proliferating OLs ($Ki67^+$ of $OLIG2^+$ cells) did not differ between CPZ Saline and CPZ Flu mice at 5 weeks (Figures 2P and 2R). These data suggest that infection did not impede proliferation of progenitor cells to the PFC but rather suppressed their maturation.

We also quantified Iba-$1^+$ microglia and $GFAP^+$ astrocytes in the CC and mPFC and found that at the time points examined, the height of gliosis occurred at peak demyelination and gradually resolved over the course of remyelination (Figure S1). However, infection did not alter the number of Iba-$1^+$ microglia and $GFAP^+$ astrocytes in either region compared to saline (Figure S1), which is consistent with the previously observed effect of infection alone.[6] Taken together, these data indicate that infection reduced the number of mature OLs in the mPFC during remyelination without affecting cell proliferation or gliosis.

To determine if infection altered the extent of remyelination, we measured mean fluorescent intensity (MFI) of myelin-associated glycoprotein (MAG) expression at time points corresponding to demyelination (5 weeks) and remyelination (5 + 1 and 5+2 weeks). Consistent with the finding that infection did not affect number of OLs in the CC, we observed no change in MAG MFI of this region between saline- and flu-inoculated mice at any time point examined (Figures 3A and 3B). In contrast, infection reduced MAG MFI at 5+1 week within the mPFC

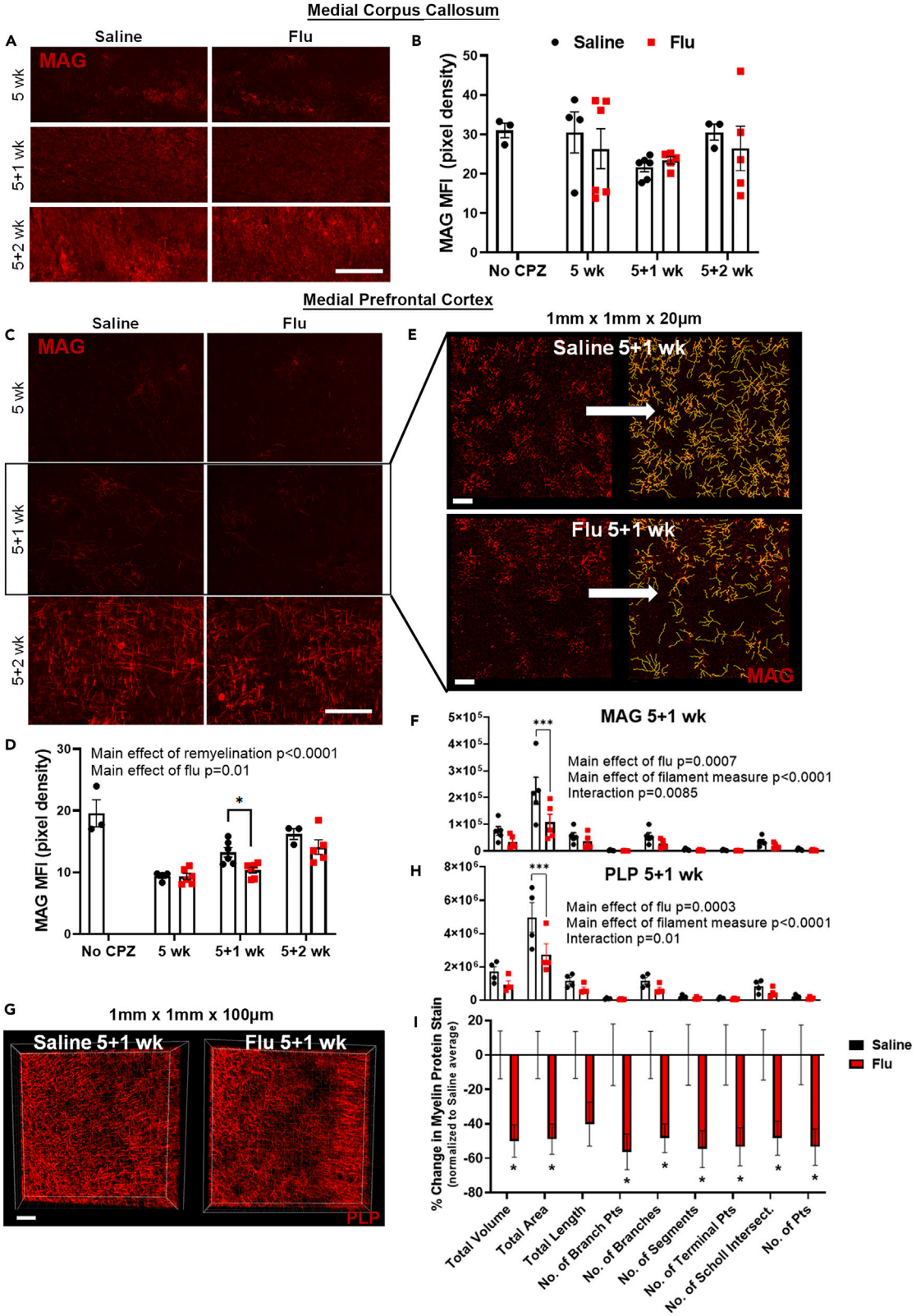
Medial Corpus Callosum
A
Saline
Flu
MAG
5 wk
5+1 wk
5+2 wk
B
Saline
Flu
MAG MFI (pixel density)
No CPZ
5 wk
5+1 wk
5+2 wk
Medial Prefrontal Cortex
C
Saline
Flu
MAG
5 wk
5+1 wk
5+2 wk
1mm x 1mm x 20µm
E
Saline 5+1 wk
Flu 5+1 wk
MAG
D
Main effect of remyelination p<0.0001
Main effect of flu p=0.01
MAG MFI (pixel density)
No CPZ
5 wk
5+1 wk
5+2 wk
F
MAG 5+1 wk
Main effect of flu p=0.0007
Main effect of filament measure p<0.0001
Interaction p=0.0085
H
PLP 5+1 wk
Main effect of flu p=0.0003
Main effect of filament measure p<0.0001
Interaction p=0.01
G
1mm x 1mm x 100µm
Saline 5+1 wk
Flu 5+1 wk
PLP
I
% Change in Myelin Protein Stain
(normalized to Saline average)
Saline
Flu
Total Volume
Total Area
Total Length
No. of Branch Pts
No. of Branches
No. of Segments
No. of Terminal Pts
No. of Scholl Intersect.
No. of Pts

**Figure 3. Infection decreased myelin density of the mPFC during remyelination**

(A) MAG expression in the medial corpus callosum (CC).
(B) Mean fluorescent intensity (MFI) of MAG in the CC.
(C) MAG expression in the medial prefrontal cortex (mPFC).
(D) MAG MFI in the mPFC. For A–D, n = 3–6 animals per condition per time point.
(E) MAG-stained mPFC at 5+1 week overlaid with filament tracer models.
(F) Select measures from filament tracer models of MAG immunofluorescence shown in E. For E and F, *n* = 5 animals per condition.
(G) CLARITY-cleared, PLP-stained mPFC at 5+1 week.
(H) Select measures from Filament Tracer models of PLP immunofluorescence shown in G. For G and H, *n* = 4 animals per condition.
(I) % change in MAG or PLP stain normalized to Saline average. For I, data analyzed by Mann-Whitney U test.
All other data analyzed by two-way ANOVA with Bonferroni correction and presented as mean ± SEM. "No CPZ" reference group was excluded from statistical analysis. All scale bars are 100μm. E and F and G and H represent two independent experiments.

(Figures 3C and 3D), which was in agreement with decreased numbers of mature OLs (Figure 2J). We asked whether three-dimensional (3D) renderings of myelinated filaments would confirm this finding. In order to establish which Imaris software-generated filament measures would be indicative of remyelination, we performed a proof-of-concept study and identified nine select measures that were decreased by CPZ-induced demyelination and subsequently increased during the remyelination period (Figure S2). Then we imaged through the 20μm MAG-stained brain section and generated 3D reconstructions of MAG immunofluorescence in the mPFC (Figure 3E). We focused our analysis on the nine remyelination-sensitive measures and found that infection decreased MAG staining (main effect of infection: $p = 0.0007$) (Figure 3F). To determine whether filament modeling using a different myelin protein would also detect an effect of infection, we repeated the experiment with a new cohort of animals and stained a larger volume of CLARITY-cleared mPFC tissue with antibody against proteolipid protein (PLP), which is expressed earlier during OL maturation and in more abundance than MAG (Figure 3G). Analysis of 3D reconstructions of PLP immunofluorescence resulted in filament measurements that scaled over 10-fold of those resulting from MAG staining, and yet the effect of infection ($p = 0.0003$) was recapitulated with the same magnitude of reduction relative to saline controls (Figure 3H). Combined analysis indicated ~50% flu-induced reductions in myelin protein stain in the mPFC at 5+1 week (Figure 3I). These data corroborated our initial result that infection delayed remyelination processes in the mPFC compared to saline controls.

## OLs and microglia exhibited increased glycolytic capacity during infection

Perturbing metabolites or metabolic pathways in OLs can result in altered function, such as dysregulated differentiation and myelination, processes that normally require upregulation of mTORC1 activity and downstream lipid biosynthetic pathways.[31] Since our data indicated that the top downregulated DEGs between Flu and Saline groups during remyelination were related to *lipid metabolism* and *lipid biosynthesis* (Table S4) we sought to determine whether infection could alter OL metabolism by employing a recently described flow cytometry-based method to assess energy metabolism with single cell resolution called SCENITH.[32] We first optimized the method for measuring metabolism of glia extracted from brain tissue (Figure S3) and validated our gating strategy to identify both mature and immature OL populations (Figure S4). Mice were inoculated with saline or flu virus at a low dose (LD Flu) or a high dose (HD Flu) (Figure 4A) and at day 8 p.i., brains were collected and metabolic changes to microglia and OLs were assessed (Figure 4B). Our gating strategy revealed seven cell populations: lymphocytes ($CD45^{hi}CD11b^{-}$), myeloid cells ($CD45^{hi}CD11b^{+}$), microglia ($CD45^{int}CD11b^{+}$), immature OLs ($CD45^{-}SOX10^{+}MAG^{-}$), mature OLs ($CD45^{-}SOX10^{+}MAG^{+}$), myelin debris ($CD45^{-}SOX10^{-}MAG^{+}$), and all other cells ($CD45^{-}SOX10^{-}MAG^{-}$) (Figure 4C). We found that cell viability was not altered by infection, with the exception of decreased percentage of mature OLs in response to HD Flu (Figure S5). However, the number of mature OLs did not change in response to LD or HD Flu, and neither did the number of immature OLs nor total OLs (Figures 4D and 4E), indicating that infection did not kill OLs. Rather, the ratio of immature OLs to mature OLs was increased in infected mice compared to saline controls in response to HD Flu (Figure 4F). This effect was not observed with LD Flu (Figure 4G). The change in proportion of mature OLs without significant change in cell number suggests that infection altered the expression of the marker used to define OL subtypes. Indeed, cellular MAG expression was decreased by ~18% in mature OLs as a result of HD Flu (Figure 4H), as we previously reported at the same viral dose.[6] Mature OLs also exhibited decreased MAG expression in response to LD Flu, but to a lesser extent (~8%; Figure 4I). To assess whether infection alone could cause OL death we generated a Sox10-Cre inducible reporter line that results in tdTomato-fluorescent OLs to fate map this cell population in a manner independent of myelin protein expression (Figures S6A–S6C). Weight loss due to infection at day 8 p.i. (~25–30%) was consistent with previous experiments with HD Flu (Figure S6D). The number of tdTomato-expressing cells differed neither in the mPFC nor CC between saline- and flu-inoculated mice (Figures S6E and S6F). Finally, we were unable to detect any cleaved caspase-3 staining at 5 weeks or 5 + 1 week in either CPZ Saline or CPZ Flu brain sections despite that staining was readily detected in cortex, CC, and hippocampus of mice at day 6 p.c. (Figures S6G–S6K), a time point in which apoptosis is maximally detected in the cuprizone model.[33] These data indicate that flu infection did not cause apoptosis at the time points examined, corroborating our finding that despite altering OL homeostasis, infection did not cause OL death.

Since puromycin acted as a proxy for global protein synthesis, we distinguished between $puromycin^{+}$ and $puromycin^{-}$ populations of viable cells (Figure S3), and termed the former "actively translating cells". Compared to saline, infection increased the proportion and protein synthesis levels of actively translating lymphocytes as well as the protein synthesis levels of myeloid cells (Figures 4J and 4K). In contrast to peripherally derived lymphocytes and myeloid cells, cells of the CNS exhibited decreased protein synthesis levels in response to HD Flu

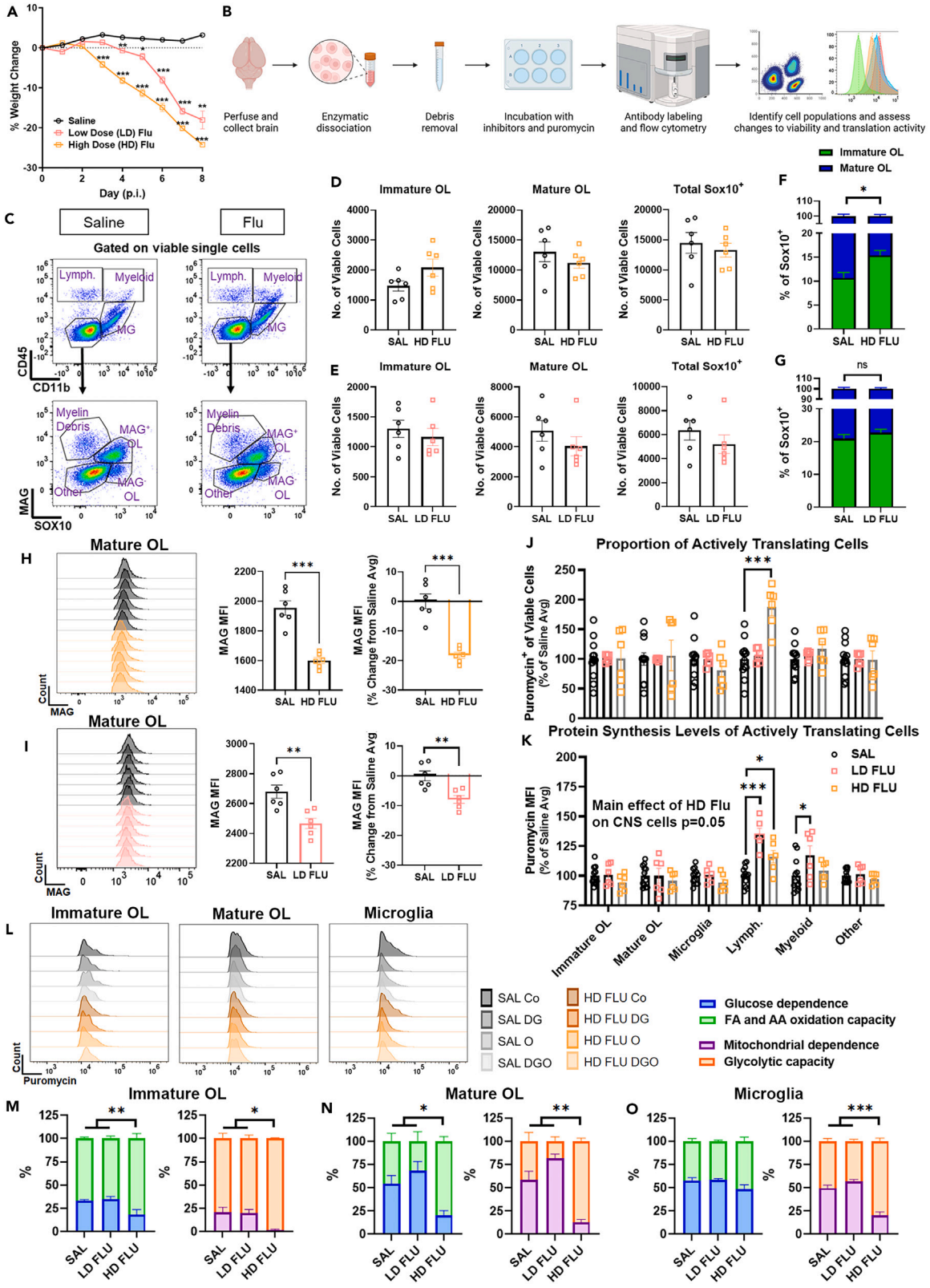
A
% Weight Change
Day (p.i.)
Saline
Low Dose (LD) Flu
High Dose (HD) Flu
B
Perfuse and collect brain
Enzymatic dissociation
Debris removal
Incubation with inhibitors and puromycin
Antibody labeling and flow cytometry
Identify cell populations and assess changes to viability and translation activity
C
Saline
Flu
Gated on viable single cells
Lymph.
Myeloid
MG
CD45
CD11b
Myelin Debris
MAG+ OL
MAG- OL
Other
MAG
SOX10
D
Immature OL
Mature OL
Total Sox10+
No. of Viable Cells
SAL HD FLU
E
Immature OL
Mature OL
Total Sox10+
No. of Viable Cells
SAL LD FLU
F
Immature OL
Mature OL
% of Sox10+
SAL HD FLU
G
ns
% of Sox10+
SAL LD FLU
H
Mature OL
Count
MAG
MAG MFI
MAG MFI (% Change from Saline Avg)
SAL HD FLU
I
Mature OL
Count
MAG
MAG MFI
MAG MFI (% Change from Saline Avg
SAL LD FLU
J
Proportion of Actively Translating Cells
Puromycin+ of Viable Cells (% of Saline Avg)
K
Protein Synthesis Levels of Actively Translating Cells
Puromycin MFI (% of Saline Avg)
SAL
LD FLU
HD FLU
Main effect of HD Flu on CNS cells p=0.05
Immature OL
Mature OL
Microglia
Lymph.
Myeloid
Other
L
Immature OL
Mature OL
Microglia
Count
Puromycin
SAL Co
SAL DG
SAL O
SAL DGO
HD FLU Co
HD FLU DG
HD FLU O
HD FLU DGO
Glucose dependence
FA and AA oxidation capacity
Mitochondrial dependence
Glycolytic capacity
M
Immature OL
%
SAL LD FLU HD FLU
N
Mature OL
%
SAL LD FLU HD FLU
O
Microglia
%
SAL LD FLU HD FLU

**Figure 4. OLs and microglia exhibited increased glycolytic capacity during infection**

(A) Percent weight change of mice post-infection (p.i.).

(B) Experimental schematic for SCENITH analysis of brain cells *ex vivo*.

(C) Gating strategy for SCENITH analysis of brain cells *ex vivo*.

(D and E) Number of viable immature OLs ($CD45^{-}SOX10^{+}MAG^{-}$), mature OLs ($CD45^{-}SOX10^{+}MAG^{+}$), and total OLs ($CD45^{-}SOX10^{+}$) from (D) HD Flu or (E) LD Flu mice.

(F and G) Proportion of immature and mature OLs of total OLs from (F) HD Flu or (G) LD Flu mice.

(H and I) MAG expression peaks of mature OLs from (H) HD Flu or (I) LD Flu mice and corresponding mean fluorescent intensity (MFI) values.

(J) Proportion of $puromycin^{+}$ (Actively Translating) of Viable Cells shown as percent of Saline average.

(K) Puromycin MFI (Protein Synthesis Levels) of Actively Translating Cells shown as percent of Saline average.

(L) Puromycin expression peaks of immature OLs, mature OLs, and microglia treated with media alone (Co), media containing 2-deoxy-D-glucose (DG), media containing oligomycin (O), or media containing both DG and O (DGO).

(M–O) Metabolic dependencies and capacities of (M) immature OLs, (N) mature OLs, and (O) microglia from HD and LD Flu mice.

$n = 6$ animals per condition with separate Saline groups for LD and HD Flu. Saline groups were combined for A, J, and K, M–O resulting in $n = 12$. For D–I, data were analyzed by Student's t test. For J and K and M–O, data analyzed by one-way ANOVA with Bonferroni correction. For K, two-way ANOVA performed on CNS cells between Saline and HD Flu and any significant main effect indicated on graph. $*p < 0.05$, $**p < 0.01$, $***p < 0.001$. Data presented as mean ± SEM.

compared to Saline controls (main effect of infection $p = 0.05$; Figure 4K). Collectively, these results were consistent with activated lymphocyte status and suppression of translation activity in cells of the CNS during infection.

Finally, we examined changes to metabolic dependencies and capacities of OLs and microglia (Figure 4L). Glycolytic capacity was increased in immature OLs, mature OLs, and microglia of HD Flu mice compared to saline controls (Figures 4M–4O). Immature and mature OLs of HD Flu mice also exhibited higher fatty acid and amino acid oxidation capacity than those of saline controls (Figures 4M and 4N). Interestingly, metabolic changes within OLs and microglia were dependent on viral dose as the lower titer of virus inoculum was not sufficient to induce alterations (Figures 4M–4O). Overall, these data demonstrate that during infection, OLs and microglia shift their metabolism toward increased glycolytic capacity in a manner dependent on sickness severity.

## Increased glycolytic capacity of OLs due to infection was in opposition to the metabolic profile induced by remyelination

To test the effect of infection on OL metabolism during remyelination, we performed SCENITH on whole brain tissue of saline- or flu-inoculated mice during remyelination (CPZ-fed) or not (age-matched, non-CPZ controls) with the same experimental design as all preceding experiments. As before, brains were collected at 5 + 0.5 weeks, a time point corresponding to peak sickness due to infection (day 8 p.i.) and partial remyelination (Figure 5A). Compared to non-CPZ controls, remyelinating groups exhibited increased percentage of microglia, lymphocytes, myeloid cells, and immature OLs (main effect of remyelination; Figures 5B and 5C). Infection increased the percentage of lymphocytes and myeloid cells, but decreased the percentage of mature OLs compared to saline (main effect of infection; Figure 5C). While the number of immature, mature, and total OLs did not differ between groups (Figure S7), there was a main effect of both infection and CPZ that indicated an increase in the ratio of immature to mature OLs (Figure 5D), as was previously observed with HD Flu (Figure 4F). Specifically, mice in the CPZ Flu group had a higher immature to mature OL ratio than mice in the CPZ Saline group (Figure 5D), suggesting that infection suppressed OL maturation during remyelination (Figure 2). Indeed, MAG expression was decreased in the mature OLs of the Flu group compared to those from the Saline group, and to a greater extent in those from the CPZ Flu group compared to the CPZ Saline group (Figure 5E).

Remyelination caused robust cell activation as evidenced by increased proportion of actively translating immature OLs, mature OLs, microglia, lymphocytes, and myeloid cells (Figure 5F). While more cells were activated during remyelination, infection severely inhibited protein synthesis levels within OLs, microglia, and myeloid cells of CPZ Flu mice compared to CPZ Saline mice (Figure 5G). We then determined metabolic dependencies and capacities of immature OLs, mature OLs, and microglia (Figure 5H). As observed previously, infection caused an increase in glycolytic capacity of immature OLs, mature OLs, and microglia (main effect of infection; Figures 5I–5K). In contrast, mature OLs exhibited increased mitochondrial dependence as a result of remyelination (main effect of remyelination; Figure 5J). Finally, we observed increased glucose dependence of microglia during remyelination (Figure 5K). Taken together, these data point toward glial activation and OL proliferation/maturation as characteristic events during remyelination, and on the converse, indicate that both translation activity and OL maturation processes were suppressed by infection.

## The metabolic profile of remyelinating OLs mirrored that of OLs from P14 mice during myelin development

To test whether increased mitochondrial dependence of mature OLs during remyelination signified a metabolic feature of endogenous OL maturation/myelination or instead reflected a characteristic of CPZ intoxication, we performed SCENITH on brains of P14 mice, an age representative of active myelin development, and compared these to mice aged >24 months, which are undergoing myelin maintenance and/or degeneration processes. As might be expected, we observed a vastly different profile of brain cell composition between P14 and aged mice. Specifically, P14 brains contained a greater number of microglia and immature OLs, but a reduced number of mature OLs compared to aged brains (Figures 6A–6C). The number of OLs did not differ between P14 and aged mice (Figure 6C), but the fraction of immature OLs in P14 mice was over 90%, while aged mice exhibited only ~10% (Figure 6D), the same as that observed in adult mice (Figures 4F and 5D). P14 mice exhibited higher numbers of actively translating immature OLs and microglia, and a lower number of actively translating mature OLs

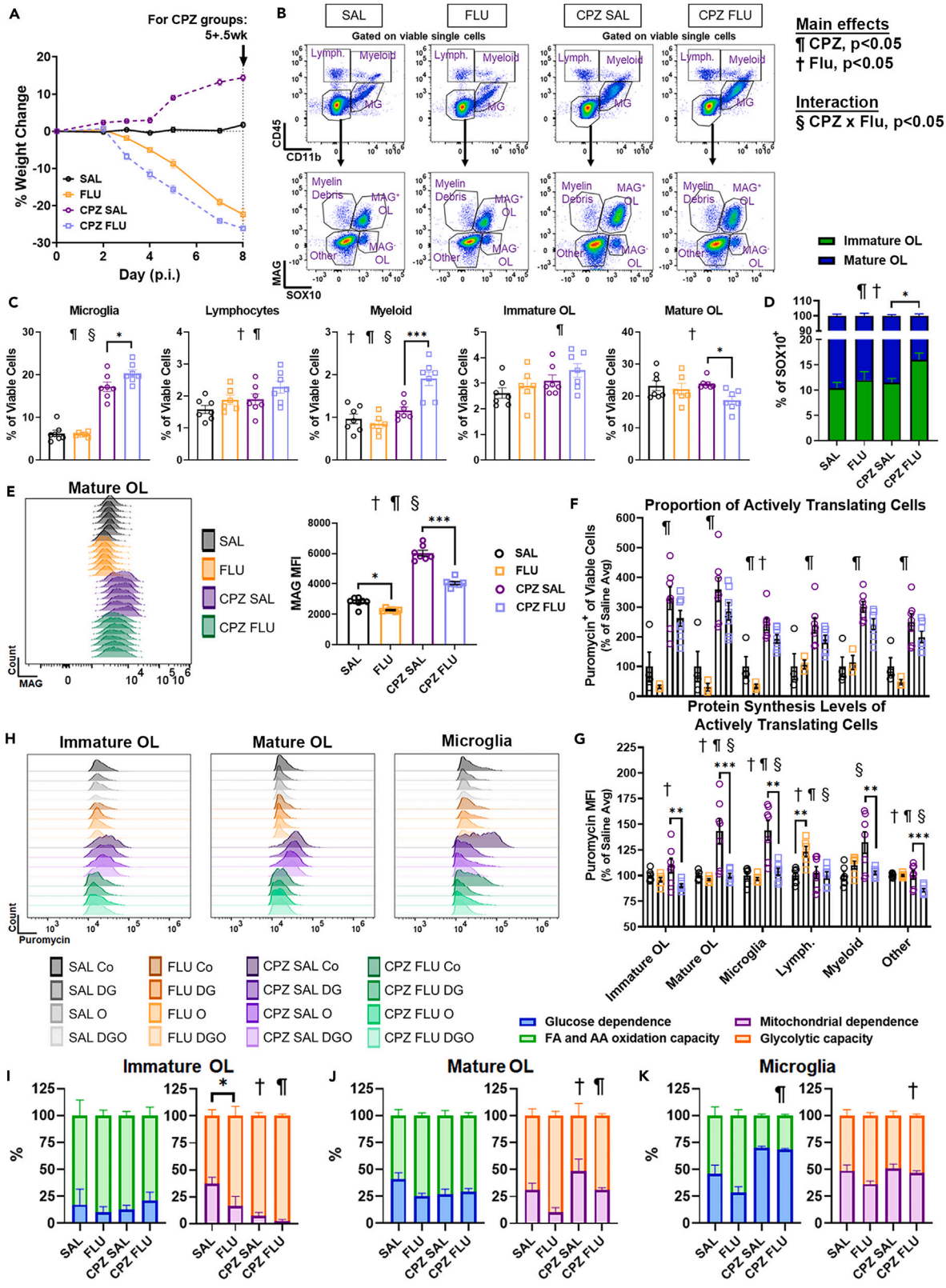
A
For CPZ groups:
5+.5wk
% Weight Change
Day (p.i.)
SAL
FLU
CPZ SAL
CPZ FLU
B
SAL
FLU
CPZ SAL
CPZ FLU
Gated on viable single cells
Lymph.
Myeloid
MG
CD45
CD11b
Myelin Debris
MAG+ OL
MAG- OL
Other
MAG
SOX10
Main effects
¶ CPZ, p<0.05
† Flu, p<0.05
Interaction
§ CPZ x Flu, p<0.05
C
Microglia
Lymphocytes
Myeloid
Immature OL
Mature OL
% of Viable Cells
D
Immature OL
Mature OL
% of SOX10+
E
Mature OL
Count
MAG
MAG MFI
F
Proportion of Actively Translating Cells
Puromycin+ of Viable Cells (% of Saline Avg)
G
Protein Synthesis Levels of Actively Translating Cells
Puromycin MFI (% of Saline Avg)
Immature OL
Mature OL
Microglia
Lymph.
Myeloid
Other
H
Immature OL
Mature OL
Microglia
Count
Puromycin
SAL Co
SAL DG
SAL O
SAL DGO
FLU Co
FLU DG
FLU O
FLU DGO
CPZ SAL Co
CPZ SAL DG
CPZ SAL O
CPZ SAL DGO
CPZ FLU Co
CPZ FLU DG
CPZ FLU O
CPZ FLU DGO
Glucose dependence
FA and AA oxidation capacity
Mitochondrial dependence
Glycolytic capacity
I
Immature OL
J
Mature OL
K
Microglia
%

**Figure 5. Increased glycolytic capacity of OLs due to infection was in opposition to the metabolic profile induced by remyelination**

(A) Percent weight change of mice post-infection (p.i.). Brains were collected at day 8 p.i., which corresponded to 5 + 0.5 weeks for cuprizone groups.

(B) Gating strategy for SCENITH analysis of brain cells *ex vivo*.

(C) Percent of viable microglia ($CD45^{int}CD11b^{+}$), lymphocytes ($CD45^{hi}CD11b^{-}$), myeloid cells ($CD45^{hi}CD11b^{+}$), immature OLs ($CD45^{-}SOX10^{+}MAG^{-}$), and mature OLs ($CD45^{-}SOX10^{+}MAG^{+}$).

(D) Proportion of immature and mature OLs of total OLs.

(E) MAG expression peaks of mature OLs and corresponding mean fluorescent intensity (MFI) values.

(F) Proportion of $puromycin^{+}$ (Actively Translating) of Viable Cells shown as percent of Saline average.

(G) Puromycin MFI (Protein Synthesis Levels) of Actively Translating Cells shown as percent of Saline average.

(H) Puromycin expression peaks of immature OLs, mature OLs, and microglia treated with media alone (Co), media containing 2-deoxy-D-glucose (DG), media containing oligomycin (O), or media containing both DG and O (DGO).

(I–K) Metabolic dependencies and capacities of (I) immature OLs, (J) mature OLs, and (K) microglia.

n = 6–7 animals per condition. Data analyzed by two-way ANOVA with Bonferroni correction and presented as mean ± SEM. $*p < 0.05$, $**p < 0.01$, $***p < 0.001$. † indicates main effect of Flu. ¶ indicates main effect of remyelination (CPZ). § indicates significant CPZ × Flu interaction.

(Figure 6E), likely due to the difference in brain cell composition. However, despite a greater number of mature OLs in the aged mice, protein synthesis levels of mature OLs were decreased compared to P14 mice (Figure 6F). In addition, despite a lower number of microglia in the aged mice, protein synthesis levels of microglia were increased compared to P14 mice (Figure 6F), reminiscent of the microglial response to CPZ (Figures 5G and 5H) and consistent with previous reports of a reactive microglial profile in aged rodents.[34–37]

We then tested metabolic responses of glia from P14 and aged mice (Figures 6G–6J) and compared these data to the average metabolic data from all saline control mice of the previous experiments as a reference for adult mice. Interestingly, microglia from aged mice exhibited higher glucose dependence and higher mitochondrial dependence than those of P14 and adult mice (Figure 6J), again reminiscent of the microglial response to CPZ (Figure 5K). Analysis of the OL fraction revealed increased glucose dependence and mitochondrial dependence of immature OLs compared to those of adult and aged mice (Figure 6H). Likewise, mature OLs of P14 mice exhibited increased mitochondrial dependence compared to those of adult mice (Figure 6I). Collectively, these data support the notion that increased mitochondrial-dependent ATP/protein production is conducive for OL maturation and/or myelination independent of any effects of CPZ.

### Increased glycolytic capacity of OLs could be phenocopied by reactive glia *in vitro*

As we consistently observed increased glycolytic capacity of OLs in response to infection, we asked whether this metabolic profile could be induced by inflammatory factors produced by activated glia. To test this premise, we cultured primary rat mixed glia and stimulated them with media containing lipopolysaccharide (LPS) or not for 24 h. We analyzed supernatants for various cytokines and chemokines and confirmed LPS-induced glial activation, evidenced by increased levels of cytokines including TNF, IL-1, and IL-6 (Figure 7A). We then performed SCENITH on media or LPS-stimulated mixed glia and by our gating strategy identified four cell populations in the mixed glia cultures: immature OLs ($CD11b^{-}SOX10^{+}PLP^{-}$), mature OLs ($CD11b^{-}SOX10^{+}PLP^{+}$), microglia ($CD11b^{+}$), and other ($CD11b^{-}SOX10^{-}$), likely astrocytes (Figure 7B). LPS treatment caused some cell death in the microglia population, and while it did not reach significance ($p = 0.06$) the number of immature OLs appeared to be reduced (Figure 7C). The number of mature OLs and total OLs were not decreased by LPS treatment (Figure 7C). However, the proportion of immature OLs of total OLs was decreased (Figure 7D), indicating preferential reduction of immature OLs over mature OLs, which has been previously reported.[38] Unlike in our infection studies,[6] LPS treatment did not reduce PLP expression in mature OLs (Figure 7E), but did reduce the proportion of actively translating cells of all populations examined (Figure 7F). Moreover, protein synthesis levels of actively translating cells were decreased in immature and mature OL populations, but not in microglia (Figure 7G). Oligomycin treatment appeared to promote cell viability of OLs and microglia upon inflammatory challenge as evidenced by number of $puromycin^{+}$ cells comparable to or even exceeding baseline media levels (Co) in the LPS treatment group (Figures 7H and 7I). This result indicated that LPS treatment increased glycolytic capacity of immature OLs, mature OLs, and microglia (Figure 7J). Additionally, OL groups exhibited increased glucose dependence in response to LPS treatment (Figure 7J). Analysis of puromycin MFI reflected similar outcomes (Figure 7K). These data demonstrate that inflammatory factors produced by activated glia are sufficient to cause increased glycolytic capacity in OLs, which was the metabolic response also observed in OLs during non-neurotropic flu infection.

## DISCUSSION

An increasing number of reports implicate myelination as a mediator of neural plasticity and dysmyelination as a cause of cognitive impairment.[39,40] Evidence shows that OLs and myelin are subject to environmental alterations including respiratory infections caused by influenza and SARS-CoV-2 viruses,[6,7] but the functional relevance of infection-induced alterations to OL homeostasis has not been fully explored. In the current study, we demonstrate that respiratory infection with influenza A virus perpetuated a demyelination- and disease-associated OL phenotype that resulted in delayed OL maturation and remyelination within the mPFC following CPZ-induced demyelination. We further show that infection reduced global translation activity and increased glycolytic capacity of OLs, an effect that was recapitulated *in vitro* with LPS stimulation of mixed glia cultures. This shift away from mitochondrial respiration toward glycolysis may be beneficial for OL survival upon inflammatory challenge, but detrimental to OL maturation. In support of this hypothesis, we found that remyelinating OLs exhibited higher dependence on mitochondrial respiration compared to non-CPZ controls. Likewise, OLs of myelinating P14 mice exhibited higher

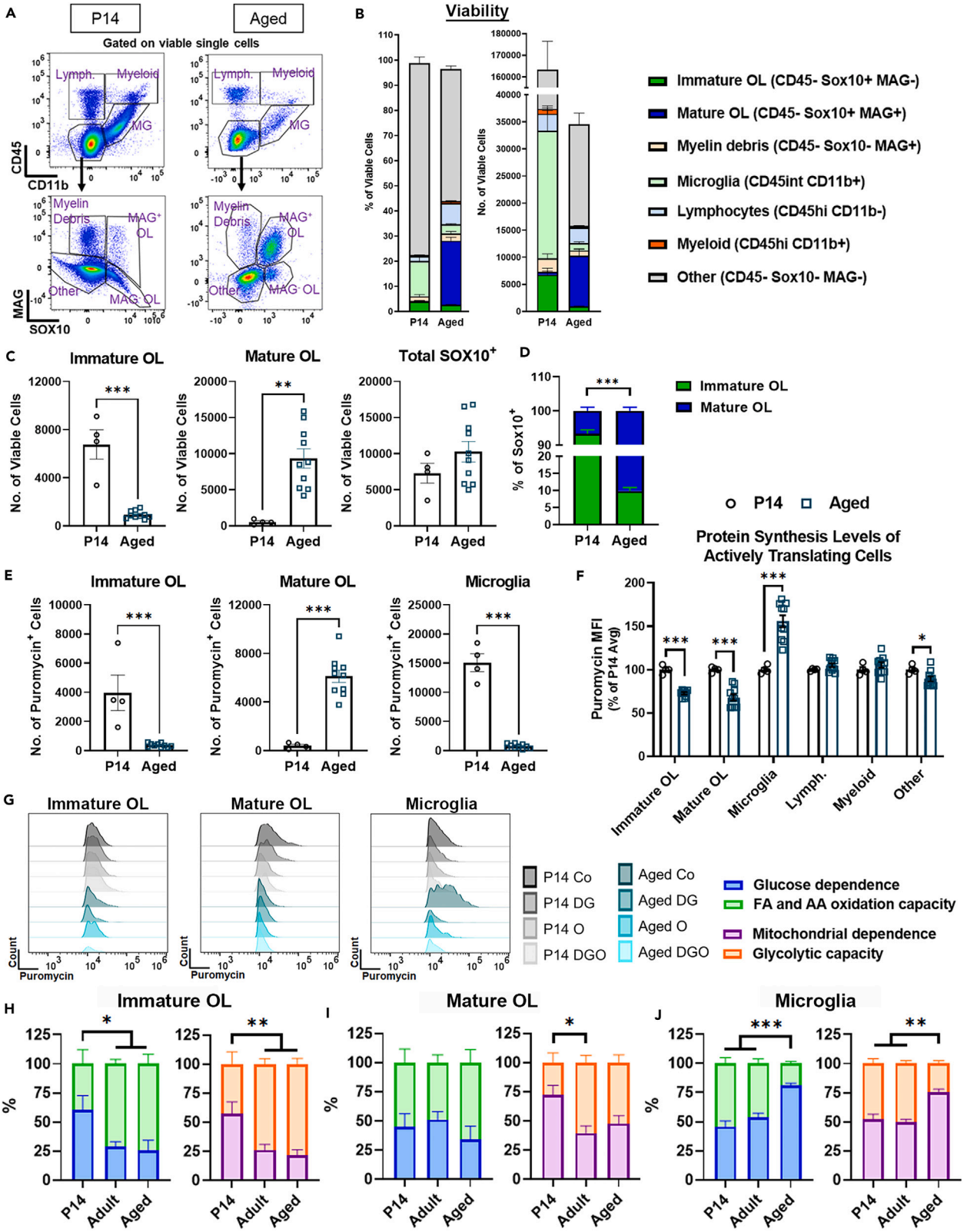
A
P14
Aged
Gated on viable single cells
Lymph.
Myeloid
MG
CD45
CD11b
Myelin Debris
MAG+ OL
Other
MAG- OL
MAG
SOX10
B
Viability
% of Viable Cells
No. of Viable Cells
P14
Aged
Immature OL (CD45- Sox10+ MAG-)
Mature OL (CD45- Sox10+ MAG+)
Myelin debris (CD45- Sox10- MAG+)
Microglia (CD45int CD11b+)
Lymphocytes (CD45hi CD11b-)
Myeloid (CD45hi CD11b+)
Other (CD45- Sox10- MAG-)
C
Immature OL
Mature OL
Total SOX10+
No. of Viable Cells
D
% of Sox10+
Immature OL
Mature OL
P14
Aged
E
Immature OL
Mature OL
Microglia
No. of Puromycin+ Cells
F
Protein Synthesis Levels of Actively Translating Cells
Puromycin MFI (% of P14 Avg)
Immature OL
Mature OL
Microglia
Lymph.
Myeloid
Other
G
Immature OL
Mature OL
Microglia
Count
Puromycin
P14 Co
P14 DG
P14 O
P14 DGO
Aged Co
Aged DG
Aged O
Aged DGO
Glucose dependence
FA and AA oxidation capacity
Mitochondrial dependence
Glycolytic capacity
H
Immature OL
I
Mature OL
J
Microglia
%
P14
Adult
Aged

**Figure 6. The metabolic profile of remyelinating OLs mirrored that of OLs from P14 mice during myelin development**

(A) Gating strategy for SCENITH analysis of brain cells *ex vivo*.

(B) Percent and number of viable cell types of brain homogenate.

(C) Number of viable immature OLs ($CD45^{-}SOX10^{+}MAG^{-}$), mature OLs ($CD45^{-}SOX10^{+}MAG^{+}$), and total OLs ($CD45^{-}SOX10^{+}$).

(D) Proportion of immature and mature OLs of total OLs.

(E) Number of puromycin$^{+}$ (actively translating) immature OLs, mature OLs, and microglia.

(F) Puromycin MFI (protein synthesis levels) of actively translating cells shown as percent of P14 average.

(G) Puromycin expression peaks of immature OLs, mature OLs, and microglia treated with media alone (Co), media containing 2-deoxy-D-glucose (DG), media containing oligomycin (O), or media containing both DG and O (DGO).

(H–J) Metabolic dependencies and capacities of (H) immature OLs, (I) mature OLs, and (J) microglia. n = 4–10 animals per condition. For H-J, the Adult group represents $n = 18$ animals, averaged from preceding experiments.

Data analyzed by Student's t test except H-J, for which one-way ANOVA with Bonferroni correction was performed. Data presented as mean ± SEM. $*p < 0.05$, $**p < 0.01$, $***p < 0.001$.

dependence on mitochondrial respiration compared to adult and aged mice. Collectively, these results indicate that respiratory viral infection antagonizes remyelination capacity, and point toward OL metabolism as a potential therapeutic target to combat remyelination failure.

Remyelination failure in demyelinating diseases such as MS is associated with increased risk of neurodegeneration[41–43] and is thought to promote disease progression.[44,45] However, the underlying causes of remyelination failure are not completely understood. Our observation that flu infection delayed OL maturation and remyelination in the PFC but not the CC points to regional differences in remyelination kinetics and is in line with animal studies that found that OL regeneration is slower and less complete in cortical gray matter compared to the CC following CPZ-induced demyelination,[46,47] perhaps allowing for a greater window of vulnerability to extrinsic influences. This is especially relevant given the association between disability and lesions within the cortex as opposed to white matter in persons with MS.[48,49] It has been suggested that the differing microenvironments of gray and white matter including differences in composition of other cell types, the extracellular matrix, and the vasculature contribute to regional differences in remyelination.[50,51] In addition, evidence suggests that impaired OL maturation, as occurs during MS, is more likely attributable to extrinsic inflammatory cues rather than intrinsic oligodendroglial factors.[52] Indeed, many studies have demonstrated the negative impact of excessive inflammation on OL differentiation *in vitro*[53–56] and remyelination capacity *in vivo*.[13–16] Pro-inflammatory glia and immune cells in human MS lesions co-present with pathological OLs.[17,29] Likewise, we found that during remyelination, infection upregulated genes associated with glial activation and response to interferon such as *Cdkn1a*, *Cd74*, *Irf7*, *Igtp*, and *H2-D1* as well as markers of OL stress such as *Plin4*, *Sult1a1*, and *Hif3a* within the same clusters. Moreover, Suhail et al. recently demonstrated that microglial activation causes alterations to OL metabolism in an experimental autoimmune encephalomyelitis (EAE) model of MS[57] in a manner that was highly consistent with the alterations we observed in the current study.

Extrinsic factors affecting OLs during infection may not be limited to pro-inflammatory cytokines and chemokines produced by activated glia. Other adverse effects imparted by respiratory viral infection, such as low oxygen and/or nutritional imbalance due to infection-induced anorexia may have also contributed to delayed remyelination observed in the current study. In support of this notion, our data show that infection highly upregulated transcripts within brain white matter during remyelination such as *Ddit4* and *Hif3a* that are indicative of DNA damage and oxidative stress as well as *Cdkn1a*, which encodes the senescence marker $p21^{CIP1}$. While further studies are needed to distinguish the mechanistic underpinnings of OL dysfunction during infection, we propose that altered OL metabolism would be the downstream crux of these various stimuli.

The data herein highlight OL metabolism as a potential therapeutic target for promoting remyelination. Dysfunctional OL metabolism has been implicated in various white matter diseases, including MS, and disease models, including CPZ.[31,58,59] Maturation and myelin generation requires substantial amounts of ATP and lipid substrate production,[60,61] and considering the additional processes of migration and proliferation that occur during remyelination, OLs certainly possess high energy demands. Perturbing metabolites or metabolic pathways in OLs can alter their function, including lactate production, differentiation, and myelination.[62–65] OLs have been shown to possess high glycolytic capacity and can maintain their viability when mitochondrial respiration is inhibited.[66] Our *in vitro* data, which show decreased OL viability in response to glycolytic inhibitor 2-deoxyglucose, but not the mitochondrial respiration inhibitor oligomycin, are in agreement with these findings and indicate that glycolysis is essential for OL survival, at least in culture. Infection-induced increase in OL glycolytic capacity could represent a programmed response in OLs to produce more lactate to support neurons,[67] to utilize themselves, or both.[68] In agreement with this hypothesis, downregulation of the OL-specific g-protein-coupled-receptor GPR17 was found promote lactate production.[69] In the current study, *Gpr17* was downregulated by infection (FDR = 0.005) in brain white matter compared to saline controls, supporting the notion of increased OL lactate production. That said, our data demonstrate that increased OL glycolytic capacity could be induced in LPS-stimulated mixed glia cultures and thus did not require neuronal input. Alternatively, a shift toward glycolysis for energy production may reflect a cellular response to minimize production of reactive oxygen species (ROS) in the mitochondria, especially considering the marked vulnerability of immature OLs to ROS toxicity.[70] With this in mind, any attempts to therapeutically target OL metabolism should account for the evolving, context-dependent metabolic needs of OLs.

While OLs possess high glycolytic capacity,[66,71] mature OLs in particular also exhibit substantial mitochondrial metabolic activity.[72] We found that remyelinating mature OLs exhibited higher mitochondrial dependence compared to mature OLs of non-CPZ controls. Independent of any effects of CPZ, we also observed increased mitochondrial dependence in OLs of P14 mice compared to those of adult and aged mice, suggesting that higher mitochondrial-dependent ATP/protein production is a conserved mechanism for OL maturation and myelination. This is in line with a study showing that administration of the bioenergetic compound creatine, which promoted mitochondrial ATP

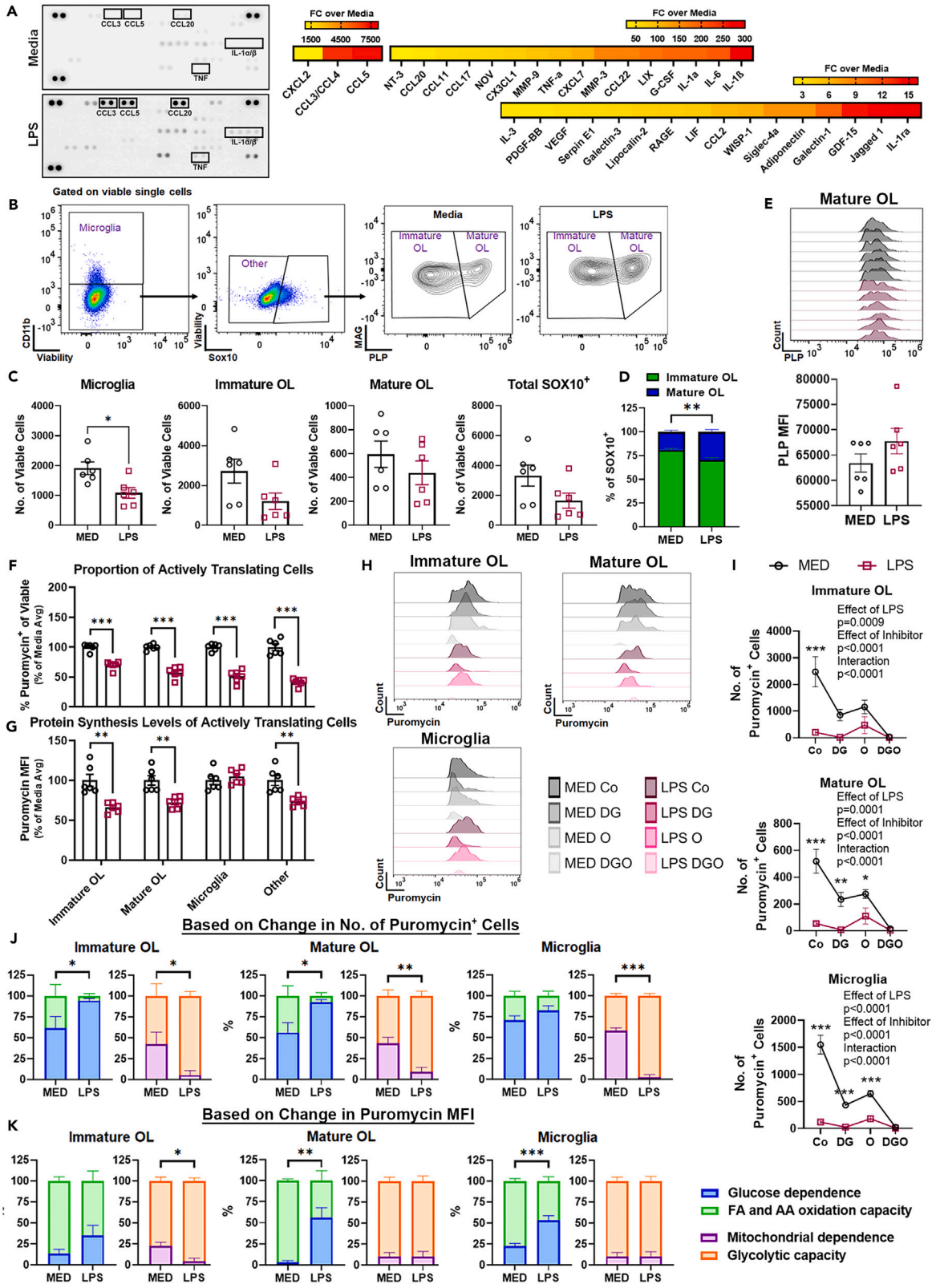
A
Media
LPS
CCL3 CCL5
CCL20
IL-1α/β
TNF
FC over Media
1500 4500 7500
CXCL2
CCL3/CCL4
CCL5
50 100 150 200 250 300
NT-3
CCL20
CCL11
CCL17
NOV
CX3CL1
MMP-9
TNF-a
CXCL7
MMP-3
CCL22
LIX
G-CSF
IL-1a
IL-6
IL-1b
3 6 9 12 15
IL-3
PDGF-BB
VEGF
Serpin E1
Galectin-3
Lipocalin-2
RAGE
LIF
CCL2
WISP-1
Siglec-4a
Adiponectin
Galectin-1
GDF-15
Jagged 1
IL-1ra
B
Gated on viable single cells
Microglia
Other
CD11b
Viability
Sox10
Media
LPS
Immature OL
Mature OL
MAG
PLP
C
Microglia
Immature OL
Mature OL
Total SOX10+
No. of Viable Cells
MED
LPS
D
Immature OL
Mature OL
% of SOX10+
E
Mature OL
Count
PLP
PLP MFI
F
Proportion of Actively Translating Cells
% Puromycin+ of Viable (% of Media Avg)
G
Protein Synthesis Levels of Actively Translating Cells
Puromycin MFI (% of Media Avg)
Immature OL
Mature OL
Microglia
Other
H
Immature OL
Mature OL
Microglia
Count
Puromycin
MED Co
MED DG
MED O
MED DGO
LPS Co
LPS DG
LPS O
LPS DGO
I
MED
LPS
Immature OL
Effect of LPS p=0.0009
Effect of Inhibitor p<0.0001
Interaction p<0.0001
No. of Puromycin+ Cells
Co DG O DGO
Mature OL
Effect of LPS p=0.0001
Effect of Inhibitor p<0.0001
Interaction p<0.0001
Microglia
Effect of LPS p<0.0001
Effect of Inhibitor p<0.0001
Interaction p<0.0001
Based on Change in No. of Puromycin+ Cells
J
Immature OL
Mature OL
Microglia
%
Based on Change in Puromycin MFI
K
Glucose dependence
FA and AA oxidation capacity
Mitochondrial dependence
Glycolytic capacity

**Figure 7. Increased glycolytic capacity of OLs could be recapitulated by reactive glia *in vitro***

(A) Cytokine/chemokine array of supernatants from Media or LPS-stimulated mixed glial cultures ($n$ = 1 pooled sample of three biological replicates).
(B) Gating strategy for SCENITH analysis of glia *in vitro*.
(C) Number of viable microglia ($CD11b^+$), immature OLs ($SOX10^+PLP^-$), mature OLs ($SOX10^+PLP^+$), and total OLs ($SOX10^+$).
(D) Proportion of immature and mature OLs of total OLs.
(E) PLP expression peaks of mature OLs and corresponding mean fluorescent intensity (MFI) values.
(F) Proportion of puromycin$^+$ (actively translating) of viable cells shown as percent of media average.
(G) Puromycin MFI (protein synthesis levels) of actively translating cells shown as percent of Media average.
(H) Puromycin expression peaks of immature OLs, mature OLs, and microglia treated with media alone (Co), media containing 2-deoxy-D-glucose (DG), media containing oligomycin (O), or media containing both DG and O (DGO).
(I) Number of puromycin$^+$ (actively translating) immature OLs, mature OLs, and microglia across inhibitor treatments.
(J and K) Metabolic dependencies and capacities of immature OLs, mature OLs, and microglia based on change in number of puromycin$^+$ cells (J) and based on change in puromycin MFI (K).
$n$ = 6 animals per condition. Data analyzed by Student's t test and presented as mean ± SEM. *$p < 0.05$, **$p < 0.01$, ***$p < 0.001$.

production of OLs in culture and increased the number of mature $CC1^+$ OLs following lysolecithin-induced demyelination.[73] The same group identified OLs as the main source of endogenous creatine synthesis in the CNS, and showed that genetic depletion of creatine synthesis results in delayed myelin development as well as delayed remyelination following lysolecithin-induced demyelination.[74] It is plausible that ATP and/or acetyl CoA production by mitochondria is conducive for providing the substantial energy and substrates OLs need to mature and myelinate.[75] However, it remains unclear whether increased mitochondrial respiration is necessary for OL maturation and myelination. In targeting OL metabolism as a treatment strategy in neurodegenerative disorders, it would be important to consider how systemic administration of bioenergetic compounds might concurrently affect the inflammatory response of other glia, especially considering sensitivity of OLs to changes in their microenvironment.

Altogether, our data demonstrate a functional consequence of altered OL homeostasis due to respiratory viral infection and identify OL metabolism as a potential therapeutic target to restore infection-induced deficits.

## Limitations of the study

Given the nature of the CPZ model, the effect of infection observed here is limited to endogenous remyelination processes in the absence of autoimmunity, and remyelination in the CPZ model does not account for the contribution of surviving mature OLs. Effects of infection on remyelination are also limited to male animals in the current study. While we define a spatial transciptomic signature of demyelination and infection during remyelination, this technique does not yet allow for further delineation of these changes at the single-cell level. Finally, while SCENITH provides advantages of *ex vivo* metabolism assessment such as the ability to assess metabolism of multiple cell types within the same sample and eliminate the extenuating processing time required to isolate cells by magnetic bead or immunopanning methods, the technique is also inherently limited by the fact that its output measures are indirect and can only be considered relative to a control group.

## STAR★METHODS

Detailed methods are provided in the online version of this paper and include the following:

- KEY RESOURCES TABLE
- RESOURCE AVAILABILITY
  - Lead contact
  - Materials availability
  - Data and code availability
- EXPERIMENTAL MODEL AND STUDY PARTICIPANT DETAILS
  - Animals
  - Primary mixed glial cultures
- METHOD DETAILS
  - Spatial transcriptomics (Visium) tissue preparation
  - Spatial transcriptomics (Visium) sequencing and data processing
  - Differential expression analysis
  - PHATE trajectory analysis
  - Immunostaining
  - CLARITY tissue clearing
  - Confocal imaging and imaris modeling analysis
  - SCENITH
  - SCENITH data analysis
  - Cytokine array
- QUANTIFICATION AND STATISTICAL ANALYSIS

## SUPPLEMENTAL INFORMATION

Supplemental information can be found online at https://doi.org/10.1016/j.isci.2024.110464.

## ACKNOWLEDGMENTS

We would like to thank the staff at the Carl R. Woese Institute for Genomic Biology and the Roy J. Carver Biotechnology Center for their technical support with Visium spatial transcriptomics. This research was supported by the National Multiple Sclerosis Society RG 1807-32053 (A.J.S.) and partially by NIH 1R21NS121741 (A.J.S.), NIH R01 AG059622 (R.W.J.), and NIH R35 GM144276 (J.L.J., A.V.K.). Research reported in this publication was supported by the National Institute of Biomedical Imaging and Bioengineering of the National Institutes of Health under Award Number T32EB019944 (A.Y.L.). The content is solely the responsibility of the authors and does not necessarily represent the official views of the National Institutes of Health. Experimental schematics were created with BioRender.com.

## AUTHOR CONTRIBUTIONS

Conceptualization, A.J.S.; methodology, A.J.S. and A.Y.L.; software, J.D. and J.L.J.; formal analysis, A.Y.L., J.D., J.L.J., and M.W.; investigation, A.Y.L.; resources, A.J.S., R.W.J., and A.K.; writing – original draft, A.Y.L.; writing – review & editing, A.Y.L., J.D., J.L.J., M.W., R.W.J., A.V.K., and A.J.S.; visualization, A.Y.L.; supervision, A.V.K., R.W.J., and A.J.S.; funding acquisition, A.V.K., R.W.J., and A.J.S.

## DECLARATION OF INTERESTS

The authors declare no competing interests.

Received: February 9, 2024
Revised: May 31, 2024
Accepted: July 2, 2024
Published: July 5, 2024

## REFERENCES

1. Sandiego, C.M., Gallezot, J.-D., Pittman, B., Nabulsi, N., Lim, K., Lin, S.-F., Matuskey, D., Lee, J.-Y., O'Connor, K.C., Huang, Y., et al. (2015). Imaging robust microglial activation after lipopolysaccharide administration in humans with PET. Proc. Natl. Acad. Sci. USA *112*, 12468–12473. https://doi.org/10.1073/pnas.1511003112.
2. Ji, P., Schachtschneider, K.M., Schook, L.B., Walker, F.R., and Johnson, R.W. (2016). Peripheral viral infection induced microglial sensome genes and enhanced microglial cell activity in the hippocampus of neonatal piglets. Brain Behav. Immun. *54*, 243–251. https://doi.org/10.1016/j.bbi.2016.02.010.
3. Jurgens, H.A., Amancherla, K., and Johnson, R.W. (2012). Influenza infection induces neuroinflammation, alters hippocampal neuron morphology, and impairs cognition in adult mice. J. Neurosci. *32*, 3958–3968. https://doi.org/10.1523/jneurosci.6389-11.2012.
4. Sadasivan, S., Zanin, M., O'Brien, K., Schultz-Cherry, S., and Smeyne, R.J. (2015). Induction of microglia activation after infection with the non-neurotropic A/CA/04/2009 H1N1 influenza virus. PLoS One *10*, e0124047. https://doi.org/10.1371/journal.pone.0124047.
5. Blackmore, S., Hernandez, J., Juda, M., Ryder, E., Freund, G.G., Johnson, R.W., and Steelman, A.J. (2017). Influenza infection triggers disease in a genetic model of experimental autoimmune encephalomyelitis. Proc. Natl. Acad. Sci. USA *114*, E6107–E6116. https://doi.org/10.1073/pnas.1620415114.
6. Louie, A.Y., Kim, J.S., Drnevich, J., Dibaeinia, P., Koito, H., Sinha, S., McKim, D.B., Soto-Diaz, K., Nowak, R.A., Das, A., and Steelman, A.J. (2023). Influenza A virus infection disrupts oligodendrocyte homeostasis and alters the myelin lipidome in the adult mouse. J. Neuroinflammation *20*, 190. https://doi.org/10.1186/s12974-023-02862-2.
7. Fernández-Castañeda, A., Lu, P., Geraghty, A.C., Song, E., Lee, M.-H., Wood, J., O'Dea, M.R., Dutton, S., Shamardani, K., Nwangwu, K., et al. (2022). Mild respiratory COVID can cause multi-lineage neural cell and myelin dysregulation. Cell *185*, 2452–2468.e16. https://doi.org/10.1016/j.cell.2022.06.008.
8. Ravenholt, R.T., and Foege, W.H. (1982). 1918 influenza, encephalitis lethargica, parkinsonism. Lancet (London, England) *2*, 860–864. https://doi.org/10.1016/s0140-6736(82)90820-0.
9. Ekstrand, J.J. (2012). Neurologic complications of influenza. Semin. Pediatr. Neurol. *19*, 96–100. https://doi.org/10.1016/j.spen.2012.02.004.
10. Xu, E., Xie, Y., and Al-Aly, Z. (2022). Long-term neurologic outcomes of COVID-19. Nat. Med. *28*, 2406–2415. https://doi.org/10.1038/s41591-022-02001-z.
11. Brown, R.A., Narayanan, S., and Arnold, D.L. (2014). Imaging of repeated episodes of demyelination and remyelination in multiple sclerosis. Neuroimage Clin. *6*, 20–25. https://doi.org/10.1016/j.nicl.2014.06.009.
12. Klotz, L., Antel, J., and Kuhlmann, T. (2023). Inflammation in multiple sclerosis: consequences for remyelination and disease progression. Nat. Rev. Neurol. *19*, 305–320. https://doi.org/10.1038/s41582-023-00801-6.
13. Goldmann, T., Wieghofer, P., Müller, P.F., Wolf, Y., Varol, D., Yona, S., Brendecke, S.M., Kierdorf, K., Staszewski, O., Datta, M., et al. (2013). A new type of microglia gene targeting shows TAK1 to be pivotal in CNS autoimmune inflammation. Nat. Neurosci. *16*, 1618–1626. https://doi.org/10.1038/nn.3531.
14. Brambilla, R., Morton, P.D., Ashbaugh, J.J., Karmally, S., Lambertsen, K.L., and Bethea, J.R. (2014). Astrocytes play a key role in EAE pathophysiology by orchestrating in the CNS the inflammatory response of resident and peripheral immune cells and by suppressing remyelination. Glia *62*, 452–467. https://doi.org/10.1002/glia.22616.
15. Brambilla, R., Persaud, T., Hu, X., Karmally, S., Shestopalov, V.I., Dvoriantchikova, G., Ivanov, D., Nathanson, L., Barnum, S.R., and Bethea, J.R. (2009). Transgenic inhibition of astroglial NF-kappa B improves functional outcome in experimental autoimmune encephalomyelitis by suppressing chronic central nervous system inflammation. J. Immunol. *182*, 2628–2640. https://doi.org/10.4049/jimmunol.0802954.
16. Moreno, M., Bannerman, P., Ma, J., Guo, F., Miers, L., Soulika, A.M., and Pleasure, D. (2014). Conditional ablation of astroglial CCL2 suppresses CNS accumulation of M1 macrophages and preserves axons in mice with MOG peptide EAE. J. Neurosci. *34*, 8175–8185. https://doi.org/10.1523/jneurosci.1137-14.2014.
17. Absinta, M., Maric, D., Gharagozloo, M., Garton, T., Smith, M.D., Jin, J., Fitzgerald, K.C., Song, A., Liu, P., Lin, J.-P., et al. (2021). A lymphocyte–microglia–astrocyte axis in chronic active multiple sclerosis. Nature *597*, 709–714. https://doi.org/10.1038/s41586-021-03892-7.
18. Smith, K.J., Blakemore, W.F., and McDonald, W.I. (1979). Central remyelination restores secure conduction. Nature *280*, 395–396. https://doi.org/10.1038/280395a0.
19. Mei, F., Lehmann-Horn, K., Shen, Y.-A.A., Rankin, K.A., Stebbins, K.J., Lorrain, D.S., Pekarek, K., A Sagan, S., Xiao, L., Teuscher, C., et al. (2016). Accelerated remyelination

during inflammatory demyelination prevents axonal loss and improves functional recovery. Elife *5*, e18246. https://doi.org/10.7554/eLife.18246.

20. Duncan, I.D., Brower, A., Kondo, Y., Curlee, J.F., Jr., and Schultz, R.D. (2009). Extensive remyelination of the CNS leads to functional recovery. Proc. Natl. Acad. Sci. USA *106*, 6832–6836. https://doi.org/10.1073/pnas.0812500106.
21. Steelman, A.J., Thompson, J.P., and Li, J. (2012). Demyelination and remyelination in anatomically distinct regions of the corpus callosum following cuprizone intoxication. Neurosci. Res. *72*, 32–42. https://doi.org/10.1016/j.neures.2011.10.002.
22. Hou, J., Zhou, Y., Cai, Z., Terekhova, M., Swain, A., Andhey, P.S., Guimaraes, R.M., Ulezko Antonova, A., Qiu, T., Sviben, S., et al. (2023). Transcriptomic atlas and interaction networks of brain cells in mouse CNS demyelination and remyelination. Cell Rep. *42*, 112293. https://doi.org/10.1016/j.celrep.2023.112293.
23. Moon, K.R., van Dijk, D., Wang, Z., Gigante, S., Burkhardt, D.B., Chen, W.S., Yim, K., Elzen, A.V.D., Hirn, M.J., Coifman, R.R., et al. (2019). Visualizing structure and transitions in high-dimensional biological data. Nat. Biotechnol. *37*, 1482–1492. https://doi.org/10.1038/s41587-019-0336-3.
24. Norkute, A., Hieble, A., Braun, A., Johann, S., Clarner, T., Baumgartner, W., Beyer, C., and Kipp, M. (2009). Cuprizone treatment induces demyelination and astrocytosis in the mouse hippocampus. J. Neurosci. Res. *87*, 1343–1355. https://doi.org/10.1002/jnr.21946.
25. Goldberg, J., Clarner, T., Beyer, C., and Kipp, M. (2015). Anatomical Distribution of Cuprizone-Induced Lesions in C57BL6 Mice. J. Mol. Neurosci. *57*, 166–175. https://doi.org/10.1007/s12031-015-0595-5.
26. Castillo-Rodriguez, M.L.A., Gingele, S., Schröder, L.J., Möllenkamp, T., Stangel, M., Skripuletz, T., and Gudi, V. (2022). Astroglial and oligodendroglial markers in the cuprizone animal model for de- and remyelination. Histochem. Cell Biol. *158*, 15–38. https://doi.org/10.1007/s00418-022-02096-y.
27. Skripuletz, T., Lindner, M., Kotsiari, A., Garde, N., Fokuhl, J., Linsmeier, F., Trebst, C., and Stangel, M. (2008). Cortical demyelination is prominent in the murine cuprizone model and is strain-dependent. Am. J. Pathol. *172*, 1053–1061. https://doi.org/10.2353/ajpath.2008.070850.
28. Samtani, G., Kim, S., Michaud, D., Hillhouse, A.E., Szule, J.A., Konganti, K., and Li, J. (2023). Brain region dependent molecular signatures and myelin repair following chronic demyelination. Front. Cell. Neurosci. *17*, 1169786. https://doi.org/10.3389/fncel.2023.1169786.
29. Falcão, A.M., van Bruggen, D., Marques, S., Meijer, M., Jäkel, S., Agirre, E., Ffrench-Constant, C., Floriddia, E.M., Vanichkina, D.P., Ffrench-Constant, C., et al. (2018). Disease-specific oligodendrocyte lineage cells arise in multiple sclerosis. Nat. Med. *24*, 1837–1844. https://doi.org/10.1038/s41591-018-0236-y.
30. Pandey, S., Shen, K., Lee, S.H., Shen, Y.A., Wang, Y., Otero-García, M., Kotova, N., Vito, S.T., Laufer, B.I., Newton, D.F., et al. (2022). Disease-associated oligodendrocyte responses across neurodegenerative diseases. Cell Rep. *40*, 111189. https://doi.org/10.1016/j.celrep.2022.111189.
31. Jeffries, M.A., McLane, L.E., Khandker, L., Mather, M.L., Evangelou, A.V., Kantak, D., Bourne, J.N., Macklin, W.B., and Wood, T.L. (2021). mTOR Signaling Regulates Metabolic Function in Oligodendrocyte Precursor Cells and Promotes Efficient Brain Remyelination in the Cuprizone Model. J. Neurosci. *41*, 8321–8337. https://doi.org/10.1523/jneurosci.1377-20.2021.
32. Argüello, R.J., Combes, A.J., Char, R., Gigan, J.P., Baaziz, A.I., Bousiquot, E., Camosseto, V., Samad, B., Tsui, J., Yan, P., et al. (2020). SCENITH: A Flow Cytometry-Based Method to Functionally Profile Energy Metabolism with Single-Cell Resolution. Cell Metab *32*, 1063–1075.e7. https://doi.org/10.1016/j.cmet.2020.11.007.
33. Hesse, A., Wagner, M., Held, J., Brück, W., Salinas-Riester, G., Hao, Z., Waisman, A., and Kuhlmann, T. (2010). In toxic demyelination oligodendroglial cell death occurs early and is FAS independent. Neurobiol. Dis. *37*, 362–369. https://doi.org/10.1016/j.nbd.2009.10.016.
34. Godbout, J.P., Chen, J., Abraham, J., Richwine, A.F., Berg, B.M., Kelley, K.W., and Johnson, R.W. (2005). Exaggerated neuroinflammation and sickness behavior in aged mice following activation of the peripheral innate immune system. Faseb. J. *19*, 1329–1331. https://doi.org/10.1096/fj.05-3776fje.
35. Henry, C.J., Huang, Y., Wynne, A.M., and Godbout, J.P. (2009). Peripheral lipopolysaccharide (LPS) challenge promotes microglial hyperactivity in aged mice that is associated with exaggerated induction of both pro-inflammatory IL-1beta and anti-inflammatory IL-10 cytokines. Brain Behav. Immun. *23*, 309–317. https://doi.org/10.1016/j.bbi.2008.09.002.
36. Perry, V.H., Matyszak, M.K., and Fearn, S. (1993). Altered antigen expression of microglia in the aged rodent CNS. Glia *7*, 60–67. https://doi.org/10.1002/glia.440070111.
37. Vailati-Riboni, M., Rund, L., Caetano-Silva, M.E., Hutchinson, N.T., Wang, S.S., Soto-Díaz, K., Woods, J.A., Steelman, A.J., and Johnson, R.W. (2022). Dietary Fiber as a Counterbalance to Age-Related Microglial Cell Dysfunction. Front. Nutr. *9*, 835824. https://doi.org/10.3389/fnut.2022.835824.
38. Kim, S., Steelman, A.J., Koito, H., and Li, J. (2011). Astrocytes promote TNF-mediated toxicity to oligodendrocyte precursors. J. Neurochem. *116*, 53–66. https://doi.org/10.1111/j.1471-4159.2010.07084.x.
39. Xin, W., and Chan, J.R. (2020). Myelin plasticity: sculpting circuits in learning and memory. Nat. Rev. Neurosci. *21*, 682–694. https://doi.org/10.1038/s41583-020-00379-8.
40. Fields, R.D. (2015). A new mechanism of nervous system plasticity: activity-dependent myelination. Nat. Rev. Neurosci. *16*, 756–767. https://doi.org/10.1038/nrn4023.
41. Kornek, B., Storch, M.K., Weissert, R., Wallstroem, E., Stefferl, A., Olsson, T., Linington, C., Schmidbauer, M., and Lassmann, H. (2000). Multiple sclerosis and chronic autoimmune encephalomyelitis: a comparative quantitative study of axonal injury in active, inactive, and remyelinated lesions. Am. J. Pathol. *157*, 267–276. https://doi.org/10.1016/s0002-9440(10)64537-3.
42. Bodini, B., Veronese, M., García-Lorenzo, D., Battaglini, M., Poirion, E., Chardain, A., Freeman, L., Louapre, C., Tchikviladze, M., Papeix, C., et al. (2016). Dynamic Imaging of Individual Remyelination Profiles in Multiple Sclerosis. Ann. Neurol. *79*, 726–738. https://doi.org/10.1002/ana.24620.
43. Franklin, R.J., ffrench-Constant, C., Edgar, J.M., and Smith, K.J. (2012). Neuroprotection and repair in multiple sclerosis. Nat. Rev. Neurol. *8*, 624–634. https://doi.org/10.1038/nrneurol.2012.200.
44. Hagemeier, K., Brück, W., and Kuhlmann, T. (2012). Multiple sclerosis - remyelination failure as a cause of disease progression. Histol. Histopathol. *27*, 277–287. https://doi.org/10.14670/hh-27.277.
45. Franklin, R.J., and Ffrench-Constant, C. (2008). Remyelination in the CNS: from biology to therapy. Nat. Rev. Neurosci. *9*, 839–855. https://doi.org/10.1038/nrn2480.
46. Baxi, E.G., DeBruin, J., Jin, J., Strasburger, H.J., Smith, M.D., Orthmann-Murphy, J.L., Schott, J.T., Fairchild, A.N., Bergles, D.E., and Calabresi, P.A. (2017). Lineage tracing reveals dynamic changes in oligodendrocyte precursor cells following cuprizone-induced demyelination. Glia *65*, 2087–2098. https://doi.org/10.1002/glia.23229.
47. Orthmann-Murphy, J., Call, C.L., Molina-Castro, G.C., Hsieh, Y.C., Rasband, M.N., Calabresi, P.A., and Bergles, D.E. (2020). Remyelination alters the pattern of myelin in the cerebral cortex. Elife *9*, e56621. https://doi.org/10.7554/eLife.56621.
48. Calabrese, M., Agosta, F., Rinaldi, F., Mattisi, I., Grossi, P., Favaretto, A., Atzori, M., Bernardi, V., Barachino, L., Rinaldi, L., et al. (2009). Cortical lesions and atrophy associated with cognitive impairment in relapsing-remitting multiple sclerosis. Arch. Neurol. *66*, 1144–1150. https://doi.org/10.1001/archneurol.2009.174.
49. Harrison, D.M., Roy, S., Oh, J., Izbudak, I., Pham, D., Courtney, S., Caffo, B., Jones, C.K., van Zijl, P., and Calabresi, P.A. (2015). Association of Cortical Lesion Burden on 7-T Magnetic Resonance Imaging With Cognition and Disability in Multiple Sclerosis. JAMA Neurol. *72*, 1004–1012. https://doi.org/10.1001/jamaneurol.2015.1241.
50. Sherafat, A., Pfeiffer, F., and Nishiyama, A. (2021). Shaping of Regional Differences in Oligodendrocyte Dynamics by Regional Heterogeneity of the Pericellular Microenvironment. Front. Cell. Neurosci. *15*, 721376. https://doi.org/10.3389/fncel.2021.721376.
51. Viganò, F., Möbius, W., Götz, M., and Dimou, L. (2013). Transplantation reveals regional differences in oligodendrocyte differentiation in the adult brain. Nat. Neurosci. *16*, 1370–1372. https://doi.org/10.1038/nn.3503.
52. Starost, L., Lindner, M., Herold, M., Xu, Y.K.T., Drexler, H.C.A., Heß, K., Ehrlich, M., Ottoboni, L., Ruffini, F., Stehling, M., et al. (2020). Extrinsic immune cell-derived, but not intrinsic oligodendroglial factors contribute to oligodendroglial differentiation block in multiple sclerosis. Acta Neuropathol. *140*, 715–736. https://doi.org/10.1007/s00401-020-02217-8.
53. Liddelow, S.A., Guttenplan, K.A., Clarke, L.E., Bennett, F.C., Bohlen, C.J., Schirmer, L., Bennett, M.L., Münch, A.E., Chung, W.-S., Peterson, T.C., et al. (2017). Neurotoxic reactive astrocytes are induced by activated microglia. Nature *541*, 481–487. https://doi.org/10.1038/nature21029.
54. Miller, B.A., Crum, J.M., Tovar, C.A., Ferguson, A.R., Bresnahan, J.C., and Beattie, M.S. (2007). Developmental stage of

oligodendrocytes determines their response to activated microglia *in vitro*. J. Neuroinflammation *4*, 28. https://doi.org/10.1186/1742-2094-4-28.

55. Pang, Y., Campbell, L., Zheng, B., Fan, L., Cai, Z., and Rhodes, P. (2010). Lipopolysaccharide-activated microglia induce death of oligodendrocyte progenitor cells and impede their development. Neuroscience *166*, 464–475. https://doi.org/10.1016/j.neuroscience.2009.12.040.
56. Moore, C.S., Cui, Q.L., Warsi, N.M., Durafourt, B.A., Zorko, N., Owen, D.R., Antel, J.P., and Bar-Or, A. (2015). Direct and indirect effects of immune and central nervous system-resident cells on human oligodendrocyte progenitor cell differentiation. J. Immunol. *194*, 761–772. https://doi.org/10.4049/jimmunol.1401156.
57. Suhail, H., Nematullah, M., Rashid, F., Sajad, M., Fatma, M., Singh, J., Zahoor, I., Cheung, W.L., Tiwari, N., Ayasolla, K., et al. (2023). An early glycolysis burst in microglia regulates mitochondrial dysfunction in oligodendrocytes under neuroinflammation. iScience *26*, 107921. https://doi.org/10.1016/j.isci.2023.107921.
58. Zhang, X., Wang, R., Hu, D., Sun, X., Fujioka, H., Lundberg, K., Chan, E.R., Wang, Q., Xu, R., Flanagan, M.E., et al. (2020). Oligodendroglial glycolytic stress triggers inflammasome activation and neuropathology in Alzheimer's disease. Sci. Adv. *6*, eabb8680. https://doi.org/10.1126/sciadv.abb8680.
59. Rone, M.B., Cui, Q.L., Fang, J., Wang, L.C., Zhang, J., Khan, D., Bedard, M., Almazan, G., Ludwin, S.K., Jones, R., et al. (2016). Oligodendrogliopathy in Multiple Sclerosis: Low Glycolytic Metabolic Rate Promotes Oligodendrocyte Survival. J. Neurosci. *36*, 4698–4707. https://doi.org/10.1523/jneurosci.4077-15.2016.
60. Harris, J.J., and Attwell, D. (2012). The energetics of CNS white matter. J. Neurosci. *32*, 356–371. https://doi.org/10.1523/jneurosci.3430-11.2012.
61. McTigue, D.M., and Tripathi, R.B. (2008). The life, death, and replacement of oligodendrocytes in the adult CNS. J. Neurochem. *107*, 1–19. https://doi.org/10.1111/j.1471-4159.2008.05570.x.
62. Saab, A.S., Tzvetavona, I.D., Trevisiol, A., Baltan, S., Dibaj, P., Kusch, K., Möbius, W., Goetze, B., Jahn, H.M., Huang, W., et al. (2016). Oligodendroglial NMDA receptors regulate glucose import and axonal energy metabolism. Neuron *91*, 119–132.
63. Lebrun-Julien, F., Bachmann, L., Norrmén, C., Trötzmüller, M., Köfeler, H., Rüegg, M.A., Hall, M.N., and Suter, U. (2014). Balanced mTORC1 activity in oligodendrocytes is required for accurate CNS myelination. J. Neurosci. *34*, 8432–8448. https://doi.org/10.1523/jneurosci.1105-14.2014.
64. Bankston, A.N., Forston, M.D., Howard, R.M., Andres, K.R., Smith, A.E., Ohri, S.S., Bates, M.L., Bunge, M.B., and Whittemore, S.R. (2019). Autophagy is essential for oligodendrocyte differentiation, survival, and proper myelination. Glia *67*, 1745–1759. https://doi.org/10.1002/glia.23646.
65. Jeffries, M.A., Urbanek, K., Torres, L., Wendell, S.G., Rubio, M.E., and Fyffe-Maricich, S.L. (2016). ERK1/2 Activation in Preexisting Oligodendrocytes of Adult Mice Drives New Myelin Synthesis and Enhanced CNS Function. J. Neurosci. *36*, 9186–9200. https://doi.org/10.1523/jneurosci.1444-16.2016.
66. Fünfschilling, U., Supplie, L.M., Mahad, D., Boretius, S., Saab, A.S., Edgar, J., Brinkmann, B.G., Kassmann, C.M., Tzvetanova, I.D., Möbius, W., et al. (2012). Glycolytic oligodendrocytes maintain myelin and long-term axonal integrity. Nature *485*, 517–521. https://doi.org/10.1038/nature11007.
67. Lee, Y., Morrison, B.M., Li, Y., Lengacher, S., Farah, M.H., Hoffman, P.N., Liu, Y., Tsingalia, A., Jin, L., Zhang, P.W., et al. (2012). Oligodendroglia metabolically support axons and contribute to neurodegeneration. Nature *487*, 443–448. https://doi.org/10.1038/nature11314.
68. Sánchez-Abarca, L.I., Tabernero, A., and Medina, J.M. (2001). Oligodendrocytes use lactate as a source of energy and as a precursor of lipids. Glia *36*, 321–329. https://doi.org/10.1002/glia.1119.
69. Ou, Z., Ma, Y., Sun, Y., Zheng, G., Wang, S., Xing, R., Chen, X., Han, Y., Wang, J., Lu, Q.R., et al. (2019). A GPR17-cAMP-Lactate Signaling Axis in Oligodendrocytes Regulates Whole-Body Metabolism. Cell Rep. *26*, 2984–2997.e4. https://doi.org/10.1016/j.celrep.2019.02.060.
70. Back, S.A., Gan, X., Li, Y., Rosenberg, P.A., and Volpe, J.J. (1998). Maturation-dependent vulnerability of oligodendrocytes to oxidative stress-induced death caused by glutathione depletion. J. Neurosci. *18*, 6241–6253. https://doi.org/10.1523/jneurosci.18-16-06241.1998.
71. Rinholm, J.E., Hamilton, N.B., Kessaris, N., Richardson, W.D., Bergersen, L.H., and Attwell, D. (2011). Regulation of oligodendrocyte development and myelination by glucose and lactate. J. Neurosci. *31*, 538–548. https://doi.org/10.1523/jneurosci.3516-10.2011.
72. Amaral, A.I., Hadera, M.G., Tavares, J.M., Kotter, M.R., and Sonnewald, U. (2016). Characterization of glucose-related metabolic pathways in differentiated rat oligodendrocyte lineage cells. Glia *64*, 21–34. https://doi.org/10.1002/glia.22900.
73. Chamberlain, K.A., Chapey, K.S., Nanescu, S.E., and Huang, J.K. (2017). Creatine Enhances Mitochondrial-Mediated Oligodendrocyte Survival After Demyelinating Injury. J. Neurosci. *37*, 1479–1492. https://doi.org/10.1523/jneurosci.1941-16.2016.
74. Rosko, L.M., Gentile, T., Smith, V.N., Manavi, Z., Melchor, G.S., Hu, J., Shults, N.V., Albanese, C., Lee, Y., Rodriguez, O., and Huang, J.K. (2023). Cerebral Creatine Deficiency Affects the Timing of Oligodendrocyte Myelination. J. Neurosci. *43*, 1143–1153. https://doi.org/10.1523/jneurosci.2120-21.2022.
75. Schoenfeld, R., Wong, A., Silva, J., Li, M., Itoh, A., Horiuchi, M., Itoh, T., Pleasure, D., and Cortopassi, G. (2010). Oligodendroglial differentiation induces mitochondrial genes and inhibition of mitochondrial function represses oligodendroglial differentiation. Mitochondrion *10*, 143–150. https://doi.org/10.1016/j.mito.2009.12.141.
76. Hao, Y., Hao, S., Andersen-Nissen, E., Mauck, W.M., Zheng, S., Butler, A., Lee, M.J., Wilk, A.J., Darby, C., Zager, M., et al. (2021). Integrated analysis of multimodal single-cell data. Cell *184*, 3573–3587.e29. https://doi.org/10.1016/j.cell.2021.04.048.
77. Crowell, H., Soneson, C., Sonrel, A., and Robinson, M. (2023). muscat: Multi-sample multi-group scRNA-seq data analysis tools. https://bioconductor.org/packages/muscat.
78. Hastie, T., and Stuetzle, W. (1989). Principal Curves. J. Am. Stat. Assoc. *84*, 502–516. https://doi.org/10.2307/2289936.
79. Street, K., Risso, D., Fletcher, R.B., Das, D., Ngai, J., Yosef, N., Purdom, E., and Dudoit, S. (2018). Slingshot: cell lineage and pseudotime inference for single-cell transcriptomics. BMC Genom. *19*, 477. https://doi.org/10.1186/s12864-018-4772-0.

## STAR★METHODS

### KEY RESOURCES TABLE

| REAGENT or RESOURCE | SOURCE | IDENTIFIER |
|---|---|---|
| Antibodies | | |
| anti-PLP (AA3; rat monoclonal) | Millipore Sigma | Cat# MABN2620-100UG; RRID: AB_3083553 |
| anti-SOX10 (SP267; rabbit monoclonal) | Abcam | Cat# ab227680; RRID:AB_2927464 |
| anti-APC (CC-1; mouse monoclonal) | Millipore Sigma | Cat#OP80; RRID:AB_2057371 |
| anti-OLIG2 (rabbit polyclonal) | Millipore Sigma | Cat# AB9610; RRID:AB_570666 |
| anti-Ki67 (SolA15; rat monoclonal) | Invitrogen | Cat# 14-5698-82; RRID:AB_10854564 |
| anti-MAG (D4G3; rabbit monoclonal) | Cell Signaling Technology | Cat# 9043; RRID:AB_2665480 |
| anti-CD16/CD32 (KT1632; rat monoclonal) | Invitrogen | Cat# MA5-18012; RRID:AB_2539396 |
| anti-CD11b-SB600 (M1/70; rat monoclonal) | Invitrogen | Cat# 63-0112-82; RRID:AB_2637408 |
| anti-CD45-PE (30-F11; rat monoclonal) | Invitrogen | Cat# 12-0451-82; RRID:AB_465668 |
| anti-MAG-AF488 (513; mouse monoclonal) | Millipore Sigma | Cat# MAB1567A4; RRID:AB_10947711 |
| anti-Puromycin-AF647 (12D10; mouse monoclonal) | Millipore Sigma | Cat# MABE343-AF647; RRID: AB_2736876 |
| anti-Iba1 (rabbit polyclonal) | FUJIFILM Wako | Cat# 019–19741; RRID:AB_839504 |
| anti-GFAP (chicken polyclonal) | Millipore Sigma | Cat# AB5541; RRID:AB_177521 |
| anti-Rabbit IgG-AF405 (goat polyclonal) | Invitrogen | Cat# A31556; RRID:AB_221605 |
| anti-Rabbit IgG-AF594 (goat polyclonal) | Invitrogen | Cat# A-11012; RRID:AB_2534079 |
| anti-Rabbit IgG-AF488 (goat polyclonal) | Invitrogen | Cat# A-11008; RRID:AB_143165 |
| anti-Mouse IgG-AF594 (goat polyclonal) | Invitrogen | Cat# A-11005; RRID:AB_2534073 |
| anti-Rat IgG-AF594 (goat polyclonal) | Invitrogen | Cat# A-11007; RRID:AB_10561522 |
| anti-Chicken IgY-AF594 (goat polyclonal) | Invitrogen | Cat# A-11042; RRID:AB_2534099 |
| Bacterial and virus strains | | |
| H1N1 influenza virus strain A/PR/8/34 | ATCC | Cat# VR-1469 |
| Chemicals, peptides, and recombinant proteins | | |
| Fixable viability dye eFluor780 | Invitrogen | Cat# 65-0865-14; |
| Triton X-100 | Millipore Sigma | Cat# T8787 |
| Hoechst 33342 | Invitrogen | Cat# H3570 |
| Fluoromount-G | Southern Biotech | Cat# 0100–01 |
| X-CLARITY mounting solution | Logos Biosystems | Cat# C13101 |
| iSpacers | SunJin Lab | https://www.sunjinlab.com/product-category/ispacer/ |
| Percoll | Cytiva | Cat# 17089101 |
| 2-deoxy-D-glucose | Sigma | Cat# D6134-5G |
| Oligomycin A | Sigma | Cat# 75351-5MG |
| Puromycin | Sigma | Cat# P7255-250MG |
| 0.05% trypsin-EDTA | Gibco | Cat# 25300054 |
| Poly-DL-ornithine hydrobromide | Sigma | Cat# P0421 |
| Lipopolysaccharide (LPS) from Escherichia coli O111:B4 | Sigma | Cat# L2630 |

(*Continued on next page*)

*Continued*

| REAGENT or RESOURCE | SOURCE | IDENTIFIER |
|---|---|---|
| Critical commercial assays | | |
| Visium Spatial Gene Expression Library Construction v1 Kit | 10x Genomics | Cat# PN-1000187 |
| Visium Tissue Optimization Kit | 10x Genomics | Cat# PN-1000193 |
| Neural Tissue Dissociation Kit (P) | Miltenyi Biotec | Cat# 130-092-628 |
| eBioscience™ Foxp3 / Transcription Factor Fixation/Permeabilization Concentrate and Diluent | Invitrogen | Cat# 00-5521-00 |
| eBioscience™ Permeabilization Buffer (10X) | Invitrogen | Cat# 00-8333-56 |
| Proteome Profiler Rat XL Cytokine Array | R&D Systems | Cat# ARY030 |
| Deposited data | | |
| 10x Spatial Transcriptomics | This paper | GSE253710 |
| Experimental models: cell lines | | |
| Primary rat mixed glia | In house | |
| Experimental models: organisms/strains | | |
| Mouse: C57BL/6J | Jackson Laboratory | Cat# 000664; RRID:IMSR_JAX:000664 |
| Mouse: B6-Tg(Sox10-icre/ERT2)388Wdr/J | Jackson Laboratory | Cat# 027651; RRID:IMSR_JAX:027651 |
| Mouse: Tg(Cnp-EGFP*)1Qrlu/J | Jackson Laboratory | Cat# 026105; RRID:IMSR_JAX:026105 |
| Mouse: B6.Cg-Gt(ROSA)26Sortm14(CAG-tdTomato)Hze/J | Jackson Laboratory | Cat# 007914; RRID:IMSR_JAX:007914 |
| Mouse: Sox10-CreERT2:Ai14 | In house | |
| Mouse: P14 C57BL/6 | In house | |
| Mouse: Aged C57BL/6 | Dr. Rodney W. Johnson, University of Illinois at Urbana-Champaign | |
| Rat: Sprague Dawley SAS SD | Charles River Laboratories, Inc. | Cat# 400; RRID:IMSR_CRL:400 |
| Oligonucleotides | | |
| Primers: Sox10cre-ERT2<br>FWD: 5′-CTG CAG CCT CCT CCA CTG-3′<br>REV: 5′-GAG ACG GAC CAA AGC CAC T-3′ | Integrated DNA Technologies | custom DNA oligos |
| Software and algorithms | | |
| ImageJ | National Institutes of Health | https://imagej.net/; RRID:SCR_003070 |
| Imaris (v9.8.0) | Bitplane | http://www.bitplane.com/imaris/imaris/; RRID:SCR_007370 |
| GraphPad Prism (v9.1.0) | GraphPad | https://www.graphpad.com/; RRID:SCR_002798 |
| BioRender | BioRender | https://www.biorender.com/; RRID: SCR_018361 |
| Invitrogen Attune NxT Cytometric Software | Invitrogen | RRID:SCR_019590 |
| FlowJo (v10.8.1) | FlowJo | https://www.flowjo.com/solutions/flowjo/; RRID:SCR_008520 |
| SpaceRanger (v1.1) | 10x Genomics | |
| SpaceRanger (v1.3) | 10x Genomics | |
| Loupe Browser (v6.0.0) | 10x Genomics | |
| R (v4.1.2) | | |
| Seurat (v4.0.6) | Hao et al.[76] | |

(*Continued on next page*)

*Continued*

| REAGENT or RESOURCE | SOURCE | IDENTIFIER |
|---|---|---|
| muscat (v1.8.0) | Crowell et al.[77] | |
| PHATE (v1.0.11) | Moon et al.[23] | |
| Slingshot (v2.7.0) | Hastie&Stuetzle[78] and Street et al.[79] | |
| DAVID Bioinformatics Resources 2021 | National Institutes of Health | david.ncifcrf.gov |
| Original R code (Data S1) | This paper | Supplemental Item |
| Other | | |
| Cuprizone Diet (0.2%, 2016) | Envigo | TD.140800 |

## RESOURCE AVAILABILITY

### Lead contact

Further information and requests for resources and reagents should be directed to and will be fulfilled by the lead contact, Andrew Steelman (asteelma@illinois.edu).

### Materials availability

This study did not generate any new unique materials.

### Data and code availability

- Spatial transcriptomic data have been deposited at the Gene Expression Omnibus (GEO) database and are publicly available as of the date of publication under accession number GSE253710.
- Original R code for spatial transcriptomic analysis is provided as a supplemental item.
- Any additional information required to reanalyze the data reported in this work is available from the lead contact upon request.

## EXPERIMENTAL MODEL AND STUDY PARTICIPANT DETAILS

### Animals

Eight-week-old male C57BL/6J mice (No. 000664) were obtained from Jackson Laboratories and fed 0.2% (w/w) cuprizone-laced diet (Teklad 140800) for 5 weeks to induce demyelination, followed by 2 weeks of normal rodent diet (Teklad 2918). Cuprizone diet was refreshed every other day. Non-cuprizone control animals were maintained on normal rodent diet throughout the experiment. Animals were housed 4 per cage under constant 12 h light/dark cycles (10am-10pm) and constant temperature and fed *ad libitum*. At 4.5 week post-cuprizone (day 31 p.c.), mice were anesthetized with 3% isoflurane and then inoculated with sterile phosphate-buffered saline (PBS) or 100 plaque-forming-units (p.f.u.) of mouse-adapted human influenza A virus (A/Puerto Rico/8/1934 H1N1) diluted in sterile PBS. Only for experiments with "Low Dose Flu", a titer of 50 p.f.u. was used. For all other experiments, a titer of 100 p.f.u. was used. The total inoculation volume was 30 μl. Animals were weighed weekly (cohort 1) or every other day (cohorts 2 and 3) and then euthanized by $CO_2$ asphyxiation at 5 wk (day 35 p.c.), 5+0.5 wk (day 39 p.c.), 5+1 wk (day 42 p.c.), and 5+2 wk (day 49 p.c.). Cohort 1 tissues were collected for spatial transcriptomics and immunostaining, cohort 2 tissues were collected for immunostaining, and cohort 3 tissues were collected for SCENITH analysis. Conditions were evenly represented in each cohort. Aged mice were at least 24 months and obtained from the National Institute on Aging (Bethesda, MD).

For the generation of male and female reporter mice exhibiting eGFP$^+$ OLs and tdTomato$^+$ microglia (Figures S3 and S4), Cnp-mEGFP (No. 026105), Tmem119-2A-CreER$^{T2}$ (No. 031820), and Csf1r$^{fl/fl}$ (No. 021212) mice were obtained from Jackson Laboratories and bred in-house. For genotyping, mice were subjected to tail biopsies upon weaning and standard DNA extraction and PCR was performed using the following primers for Cnp: 5′-GTG CTT TAA GTT AGG CTT GGG-3′ and 5′-GTA GGT CAG GGT GGT CAC GA-3′, Tmem119-Cre: 5′-ATC GCA TTC CTT GCA AAA GT-3′ (mutant forward) and 5′-CAG TAT GTG GGG TCA CTG AAG A-3′ (WT forward) and 5′-ACT TGG GGA GAT GTT TCC TG-3′ (common reverse), Csf1r: 5′-CAT GGC TGT GGC CTA GAG A -3′ and 5′-GGA CTA GCC ACC ATG TCT CC -3′. Cnp-mEGFP express a membrane-anchored green fluorescent protein driven by the Cnp promoter constitutively. Recombination of loxP sites flanking Csf1r by Tmem119-Cre was induced at 7-9 weeks of age by oral gavage with tamoxifen (Sigma #T5648) dissolved in filtered corn oil (Sigma #C8267). A stock solution of 25mg/ml was prepared by dissolving tamoxifen into corn oil on an orbital shaker (Thermo Scientific Max Q 4000) at 37°C for several hours protected from light, and then sonicating in brief pulses to ensure complete solubilization. Tamoxifen was administered at a dose of 5mg in a 200ul volume per day for 5 consecutive days.

For the generation of male and female Sox10 Cre-driven reporter mice (Figure S6), Sox10-iCreER$^{T2}$ mice (No. 027651) and Ai14 mice (No. 007914) were obtained from Jackson Laboratories and bred in-house. For genotyping, mice were subjected to tail biopsies upon weaning and standard DNA extraction and PCR was performed using the following primers for Sox10-Cre: 5′-CTG CAG CCT CCT CCA CTG-3′ and 5′-GAG ACG GAC CAA AGC CAC T-3′. Recombination was induced at 7-9 weeks of age by oral gavage of tamoxifen dissolved in corn oil as described above. Inoculations were performed after a one week washout period on 8-10 wk old mice as described above.

### Primary mixed glial cultures

Primary mixed glia were isolated from male and female P0-P2 Sprague-Dawley rat pups, which were obtained from Charles River Laboratories (No. 400). Pups were euthanized by decapitation, brains collected, and meninges removed under a dissecting microscope (Leica EZ4). Tissue was triturated through a 10ml serological pipette and enzymatically digested with Accutase (Gibco #A1110501) for 15 minutes at 37°C. The cells were then washed with Dulbecco's modified eagle medium (DMEM) containing 10% heat-inactivated fetal bovine serum (FBS) and 1% penicillin-streptomycin, filtered through a sterile 70-μm filter, and seeded onto poly-DL-ornithine coated 6-well plates for experiments using mixed glia. Cells were maintained in DMEM with 4.5 g/L glucose, L-glutamine, and sodium pyruvate (Corning #10013CV) supplemented with 10% FBS (R&D Systems #S11150H), penicillin (100 U/ml) and streptomycin (100 μg/ml; Gibco #15140-122). Each pup brain was used to seed one 6-well plate coated with poly-DL-ornithine (Sigma #P0421) and each pup was considered a biological replicate as brains were processed and cultured individually. After mixed glial cultures reached confluence, they were treated with serum-free DMEM containing LPS (100ng/ml; Sigma) or not for 24 hours. Primary mixed glial cultures were not tested for mycoplasma contamination as incidence is minimal for primary cultures.

All animal care protocols were in accordance with National Institutes of Health Guidelines for Care and Use of Laboratory Animals and were approved by the University of Illinois Laboratory Animal Care and Use Committee under protocol #22083.

## METHOD DETAILS

### Spatial transcriptomics (Visium) tissue preparation

At 5 wk and 5+0.5 wk p.c., corresponding to peak demyelination and partial remyelination, respectively, brains were harvested, bisected sagittally, trimmed rostral to the fornix and caudal to the splenium of the CC, immediately frozen in a bed of finely crushed dry ice, and then embedded in Tissue-Tek® O.C.T. Compound (Sakura #4583) in a dry ice-ethanol slurry. Sagittal sections were cut on a cryostat microtome (Leica CM 1950) at 10 μm thickness and within 0-0.5 mm from the midline. Fresh, frozen sections were placed on slides (one replicate of each treatment per slide) containing spatially-barcoded oligonucleotide probes in a 6.5 x 6.5 mm area and processed according to manufacturer's instructions (Visium Spatial Gene Expression kit V1, 10x Genomics). Briefly, tissues were fixed, stained, and permeabilized on the slide. cDNA libraries were synthesized from captured RNA, resulting in spatially-resolved brain transcriptomes of mice from four conditions (n=3 animals per condition): "Normal" (control diet), "Demyelinated" (cuprizone diet, 5 wk p.c.), "Saline" (cuprizone diet, PBS-inoculated, 5+0.5 wk p.c.), and "Flu" (cuprizone diet, flu-inoculated, 5+0.5 wk p.c.).

### Spatial transcriptomics (Visium) sequencing and data processing

The cDNA libraries were pooled and sequenced on two S4 2X150nt lanes in a NovaSeq 6000 (Illumina); read 1 (cell barcode + Unique Molecular Identifier (UMI) index) was trimmed to 28 nt and samples were demultiplexed using SpaceRanger (v1.1, 10X Genomics). Each sample was run through spaceranger count (SpaceRanger v1.3, 10X Genomics) to align reads to a custom-made reference of NCBI's GRCm39 genome, Annotation Release 109 plus Influenza A virus (A/Puerto Rico/8/1934(H1N1)) genome assembly ViralMultiSegProj15521 (GCF_000865725.1); reads were collapse to unique UMIs and counted per gene per spot. No viral gene expression was detected in any spots in any sample. The individual samples were also aggregrated using spaceranger aggr with –normalize=none to generate a .cloupe to explore results using 10X Genomic's Loupe Browser.

The spaceranger count outputs per sample were read into R (v4.1.2) using Seurat (v4.0.6)[76] for further analysis. All samples were normalized together using SCTransform and then Principle Components Analysis was run on the top 3000 most variable genes. The first 30 PCs were run through the Uniform Manifold Approximation and Projection (UMAP) dimensional reduction technique; samples did not segregate in UMAP space (Figure 1C) so no integration was necessary. The first 30 PCs were also used to cluster the spots using Shared Nearest Neighbors with resolution = 0.1.

Spatial transcriptomic data have been deposited at the Gene Expression Omnibus (GEO) database and are publicly available as of the date of publication under accession number GSE253710.

### Differential expression analysis

Differences in expression between treatments within each cluster (except cluster 5) was done using the muscat package's (v1.8.0)[77] "psuedobulk" method using a model of ~ Trt + slide to correct for subtle slide differences. All 6 possible pairwise comparisons between the 4 treatment groups, Demyel. vs. Norm., Saline vs. Norm., Flu vs. Norm., Demyel. vs. Flu, Demyel. vs. Saline, and Flu vs. Saline, were pulled from the model using method = "edgeR" and a global False Discovery Rate adjustment was used so that genes with the same raw p-value would get the same FDR p-value no matter what cluster it was in. Results for any gene with raw p-value < 0.001 are provided in Table S2. Results shown in Figure 1 were further filtered with a global FDR cutoff of 0.05. Results for genes altered by infection shown in Table S3 had FDR<0.05 and FC>2 in at least one of clusters 1 and 2. Gene ontology analyses were performed on upregulated and downregulated genes that achieved an FDR<0.05 using DAVID Bioinformatics Resources 2021 (david.ncifcrf.gov).

### PHATE trajectory analysis

All twelve samples were analyzed together. The set of 3000 variable genes was exported as a spotXexpression matrix with sample and treatment information included. The matrix was read into PHATE(v 1.0.11)[23] for dimensional reduction, using default values. Trajectory analysis was

then run on the PHATE output with Slingshot (v 2.7.0).[78,79] As no single cluster was the obvious base, the PHATE projection was examined and a selection of spots that was the visual base of the graph was renamed "cluster x" and used as the starting cluster. (phate1 > -0.015, phate1< 0.005 & phate2 < -0.01). This resulted in 4 trajectories, one that was composed of mainly clusters 1,2, and 4, one with cluster 6, one with cluster 3, and one with clusters 0,5, and 7. The trajectories generated in Slingshot were measured in pseudo-time, with a single pseudo-time assigned to each spot for each trajectory it is a member of. Trajectory L1 was visualized as a heatmap on the Visium sections.

## Immunostaining

Brains were harvested and prepared for immunostaining as previously described.[6] Sagittal brain sections of 20 μm thickness were rehydrated in PBS for 20 min and then blocked with PBS containing 5% goat serum and 0.3% Triton-X 100 (PBST) for 1 h at room temperature. Tissue sections were then incubated with the following primary antibodies at 4°C overnight: anti-APC clone CC1 (1:200; Calbiochem #OP80), anti-SOX10 (1:200; Abcam #AB227680), anti-GFAP (1:1000; EMD Millipore #AB5541), and anti-Iba1 (1:1000; FUJIFILM Wako #019-19741), anti-OLIG2 (1:200; EMD Millipore #AB9610), anti-Ki-67 clone SolA15 (1:100; Thermo #14-5698-82), and anti-MAG (1:100; Cell Signaling #9043). After washing with PBST for three rounds of 5 min each, tissues were incubated with fluorophore-conjugated secondary antibody at 1:1000 dilution for 1 h at room temperature before washing again with PBST. The following secondary antibodies were used: goat anti-mouse Alexa Fluor™ 594 (Thermo #A11005), goat anti-rat Alexa Fluor™ 594 (Thermo #A11007), goat anti-rabbit Alexa Fluor™ 488 (Thermo #A11008), goat anti-rabbit Alexa Fluor™ 594 (Thermo #A11012), goat anti-chicken Alexa Fluor™ 594 (Thermo #A11042), goat anti-chicken Alexa Fluor™ 488 (Thermo #A11039). Tissues were counter-stained with Hoechst 33342 (1:5000; Thermo #H3570), washed in PBST, and mounted in Fluoromount-G® (Southern Biotech #0100–01).

Images (1mm x 0.75mm) were acquired on a ZOE™ Fluorescent Cell Imager (BioRad #1450031) with a 20x objective and resolution of 2.585 pixels/μm. Cells were counted manually using the "Multi-point" tool on ImageJ (National Institutes of Health) and normalized to the area quantified in $mm^2$. For mean fluorescent intensity (MFI) measurements, the "Polygon selections" tool was used to manually select the area of interest and "mean gray value" was used as the readout. For each animal, counts from 2-3 tissue sections were averaged per region, and 3-12 animals were averaged per condition per time point.

## CLARITY tissue clearing

Brains were harvested and processed for CLARITY as previously described.[6] Brains were harvested, bisected, and post-fixed in PBS containing 4% PFA (w/v) overnight at 4°C. Halved brains were then incubated in PBS overnight at 4°C. Next, 1mm sagittal sections were generated using a sagittal mouse brain matrix (Kent Scientific). Each section was then submerged in hydrogel solution containing final concentrations of 3% acrylamide (Bio-Rad #161-0140), 3% formaldehyde (Electron Microscopy Sciences #19200), and 0.25% VA-044 thermal initiator (m/v; Wako Chemicals #NC0632395) for 24–48 h at 4°C. Incubated tissues were polymerized in hydrogel solution at -90 kPa for 3 h at 37°C, washed three times with PBS, then actively cleared by electrophoresis using X-CLARITY™ Tissue Clearing System (Logos Biosystems). After lipid clearing, the tissues were incubated in PBS containing anti-PLP clone AA3 (EMD Millipore #MABN2620), 0.1% Triton-X 100 (v/v; Sigma Aldrich #T8787; PBST), 2% goat serum (Abcam #ab7481), and 0.01% sodium azide (Sigma Aldrich #S2002) for 3 days at 50 rpm and 37°C on an orbital shaker (Thermo Scientific Max Q 4000). After washing for 24 hours in PBST, tissues were stained with goat anti-rat IgG (H + L) cross-adsorbed Alexa Fluor 594 secondary antibody (diluted 1:100 in PBST, Thermo Scientific #A-11007) under the same conditions as the primary step and subsequently washed for 24 h in PBST. Tissues were then incubated in X-CLARITY mounting solution (RI = 1.46, Logos Biosystems #C13101) for 24–48 h before mounting between coverslips (Corning #2980-245) using iSpacers® (SunJin Lab).

## Confocal imaging and imaris modeling analysis

Images were acquired with a Zeiss LSM 710 Confocal Microscope with a 10x objective as previously described.[6] Z-stacks were acquired at 1μm steps in the Z direction, 0.48μm/pixel in the X, Y-plane, and 0.95μsec pixel dwell time, resulting in whole datasets of 850 × 850μm in the X, Y-plane and 100μm in the Z direction for PLP-stained tissues or 20μm in the Z direction for MAG-stained tissues. Three-dimensional (3D) models were rendered with Imaris x64 software (ver. 9.8.0, Bitplane, Oxford Instruments) and analyzed with the software's automated Filament Tracer module. All images were analyzed in the same fashion by a rater blinded to condition.

## SCENITH

The following describes how SCENITH was performed for brain cells *ex-vivo* as adapted from the original method.[32] Deviations to accommodate optimization tests or *in-vitro* applications are noted. Brains were collected and digested as previously described.[6] Briefly, brain tissue was enzymatically digested using Neural Tissue Dissociation Kit with papain (Miltenyi #130-092-628) following manufacturer's instructions for manual dissociation, passed through a sterile 70μm filter using a 3ml syringe plunger, and then pelleted through sterile PBS containing 30% Percoll. For mechanical digestion (optimization test; Figure S3), the same steps were followed without the use of papain. Cells were resuspended in 1200μl of plating media: DMEM with 4.5 g/L glucose, L-glutamine, and sodium pyruvate (Corning #10013CV) containing 0.25% w/v bovine serum albumin (Sigma #A9418). Glucose, glutamine, and pyruvate were included in plating media to promote cell viability; since cells may uptake pyruvate and bypass glycolysis, metabolism results should be considered relative to the control group, not as absolute values. Working solutions of each inhibitor (3x) and puromycin (10x) were prepared from stock solutions as indicated in the table below immediately before use and kept on ice.

| Reagent | Vehicle | Stock conc. | Working conc. | Final conc. (1x) |
|---|---|---|---|---|
| 2-deoxy-D-glucose (Sigma # D6134-5G) | Sterile $ddH_2O$ | 1M | 300mM (3x) | 100mM |
| Oligomycin A (Sigma #75351-5MG) | DMSO | 1mM | 3μM (3x) | 1μM |
| Puromycin (Sigma # P7255-250MG) | Sterile $ddH_2O$ | 10mg/ml | 100μg/ml (10x) | 10μg/ml |

Plating media and inhibitor working solutions (3x) were added to appropriate wells in 6-well plates (CytoOne #CC7682-7506) as indicated in the table below.

| Condition | Volume of Plating Media | Volume of DG (3x) | Volume of O (3x) | Volume of Puromycin (10x) |
|---|---|---|---|---|
| Co | 600μl | 0μl | 0μl | 100μl |
| DG | 300μl | 300μl | 0μl | 100μl |
| O | 300μl | 0μl | 300μl | 100μl |
| DGO | 0μl | 300μl | 300μl | 100μl |

Cells were added to the side of each well in a volume of 300μl, resulting in ~$10^5$ cells per condition for a whole brain. For *in-vitro* experiments, cultured cells were washed with plain media after LPS treatment and then media and inhibitors were added directly to wells containing cultured cells. Plates were swirled to thoroughly mix well contents. After a 10 min incubation at 37°C, puromycin was added in a volume of 100μl to each well for a final volume of 1ml per well and swirled to evenly distribute. After an additional 30 min incubation at 37°C, cells were collected into 2ml microcentrifuge tubes. Wells were washed with 1 ml cold PBS to detach any adherent microglia/myeloid cells and collected. For *in-vitro* experiments, after incubation with inhibitors and puromycin, media was aspirated, cells were washed with cold PBS, and detached by 1 min incubation with 0.05% trypsin-EDTA (Thermo #25300054) at 37°C and tapping the plate by hand. Trypsin activity was quenched by addition of plating media. For tube incubation (optimization test; Figure S3), cells were incubated with inhibitors and puromycin in 15ml conical tubes (Corning #430791) instead of 6-well plates.

Cells were pelleted at 400 xg for 5 min at 4°C, decanted, and incubated with anti-CD16/CD32 clone KT1632 (Thermo #MA5-18012) in flow buffer (PBS containing 2% v/v FBS) for 10 min on ice. Cells were then incubated for 20 min on ice with the following surface markers diluted in flow buffer: anti-CD45 clone 30-F11, PE conjugate (Thermo #12-0451-82), anti-CD11b clone M1/70, Super Bright 600 conjugate (Thermo #63-0112-82), and eFluor 780 fixable viability dye (Thermo #65-0865-14). Cells were washed with 1ml of cold PBS and then incubated overnight in Foxp3 fixation/permeabilization buffer (Thermo #00-5521-00) according to manufacturer's instructions. The following day, 1ml of permeabilization buffer was added to samples (Thermo #00-8333-56), which were then centrifuged at 400 xg for 5 min, decanted, and incubated for 1 hr on ice with the following intracellular markers diluted in permeabilization buffer: anti-MAG clone 513, Alexa Fluor 488 conjugate (EMD Millipore #MAB1567A4), anti-Puromycin clone 12D10, Alexa Fluor 647 conjugate (EMD Millipore #MABE343-AF647), anti-SOX10 clone SP267 (Abcam #AB227680), and anti-PLP clone AA3 (EMD Millipore #MABN2620). Cells were washed with permeabilization buffer and subsequently incubated for 1 hr on ice with appropriate fluorophore-conjugated secondary antibody: goat anti-rabbit Alexa Fluor™ 405 (Thermo # A-31556) and goat anti-rat Alexa Fluor™ 594 (Thermo #A11007). After washing with permeabilization buffer, cells were resuspended in 300μl of flow buffer and data were acquired on an Attune NxT cytometer with Invitrogen Attune NxT Cytometric Software (Thermo).

## SCENITH data analysis

SCENITH results were analyzed using FlowJo software (ver. 10.8.1.). Gates were determined using fluorescence minus one (FMO) stained samples, including puromycin$^+$ events (Figure S3). Metabolic dependencies and capacities were calculated by change in number of puromycin$^+$ cells as well as change in puromycin MFI (Figure S3). Glucose dependence (%) was defined as the difference in number of puromycin$^+$ cells between media control (Co) and 2-deoxy-D-glucose (DG) treatment divided by the difference in number of puromycin$^+$ cells between Co and treatment with both inhibitors combined (DGO). Mitochondrial dependence (%) was defined as the difference in number of puromycin$^+$ cells between Co and oligomycin (O) treatment divided by the difference between Co and DGO. Of the puromycin$^+$ cell populations, glucose dependence and mitochondrial dependence were calculated by change in puromycin MFI. Unless otherwise noted, metabolism results are shown for change in puromycin MFI. The complementary measures of glucose dependence and mitochondrial dependence, as defined by Arguello et al., are fatty acid/amino acid oxidation capacity and glycolytic capacity, respectively.[32] For any one measure, the lower limit was capped at 0% and the upper limit was capped at 100%. Metabolic measures are presented as % and considered relative, not absolute. Geometric mean was used as the readout for puromycin MFI except for DGO, for which mode was used to avoid an artificial increase in geometric mean due to reduction in total number of viable cells for that condition. For visualization purposes only, counts were normalized to mode for representative peaks.

### Cytokine array

To confirm LPS-induced glial activation and to gain insight into which secreted factors from reactive glia may be acting to alter OL metabolism, we analyzed supernatants for various cytokines and chemokines using the Proteome Profiler Rat XL Cytokine Array (R&D #ARY030). Supernatants from rat mixed glia cultures stimulated with LPS for 24 hours were collected and centrifuged at 1000 xg for 5 min to remove any cell debris. Supernatants from three biological replicates were combined for each condition (n=1 pooled sample per condition) and analyzed per manufacturer's instructions.

## QUANTIFICATION AND STATISTICAL ANALYSIS

R software (v4.1.2) was used for statistical analysis of Visium spatial data using packages Seurat (v4.0.6) for normalization, PCA, UMAP and clustering, and muscat (v1.8.0) for differential expression testing.

GraphPad Prism software (ver. 9.1.0) was used to execute all other statistical analyses and to create graphs. For weight change data, repeated-measures mixed effects analyses with fixed effects of time and diet, matched values by time, and Bonferroni correction for multiple comparisons were performed. Statistical analyses for cell counts and SCENITH data were performed with two-way ANOVA with Bonferroni multiple comparisons test with fixed effects of cuprizone (remyelination) and infection. For analysis of data between three groups, one-way ANOVA with Bonferroni correction was performed. For all other analysis between two groups, Student's t-test was performed if normality and homoscedasticity assumptions were met. If not, non-parametric Mann-Whitney U test was performed. Data were only excluded if values were identified as statistical outliers by the ROUT method (Q=1%) performed using Prism software. P values less than 0.05 were considered statistically significant. Data are represented as mean $\pm$ SEM. Statistical tests used and sample size n are indicated in figure legends. In all cases, n represents number of individual animals.